THz Dynamic Nuclear Polarization NMR

THz Dynamic Nuclear Polarization NMR

Emilio A. Nanni, *Student Member, IEEE*, Alexander B. Barnes, *Student Member, IEEE,* Robert G. Griffin, and Richard J. Temkin, *Fellow, IEEE*

***Abstract*— Dynamic Nuclear Polarization (DNP) increases the sensitivity of NMR spectroscopy by using high frequency microwaves to transfer the polarization of the electrons to the nuclear spins. The enhancement in NMR sensitivity can amount to a factor of well above one hundred, enabling faster data acquisition and greatly improved NMR measurements. With the increasing magnetic fields (up to 23T) used in NMR research, the required frequency for DNP falls into the THz band (140 to 600 GHz). Gyrotrons have been developed to meet the demanding specifications for DNP NMR, including power levels of 10 to 100 Watts; frequency stability of a few MHz; and power stability of 1% over runs that last for several days to weeks. Continuous gyrotron frequency tuning of over 1 GHz has also been demonstrated. The complete DNP NMR system must include a low loss transmission line; an optimized antenna; and a holder for efficient coupling of the THz radiation to the sample. This paper describes the DNP NMR process and illustrates the THz systems needed for this demanding spectroscopic application. THz DNP NMR is a rapidly developing, exciting area of THz science and technology.**

***Index Terms*— high power terahertz radiation, terahertz, gyrotron, DNP, NMR**

I. Introduction

Nuclear Magnetic Resonance (NMR) is the preferred spectroscopic approach for the solution of problems in many areas of science, including physics, chemistry, biology, materials science, and medicine. The excellent resolution of NMR is a consequence of long nuclear relaxation times that are in turn due to the small magnetic moments of the nuclear spins that couple weakly to the surrounding lattice. The small size of these magnetic moments however leads to reduced sensitivity in NMR experiments.

Dynamic nuclear polarization (DNP) increases the sensitivity of NMR by transferring the large spin polarization from stable paramagnetic centers to the nuclear spin reservoir [1]. In 1953 Overhauser [2] proposed that it was possible to transfer polarization to nuclei from electrons in metals by saturating the electron transition. This technique was experimentally verified by Carver and Slichter [3]. The DNP approach to NMR was extended to solid dielectrics by Abragam and Proctor [4] who first characterized the solid effect (SE). In the 1980s, Wind, Yannoni, Schaefer and colleagues [5-7] performed DNP in conjunction with magic-angle-spinning (MAS) NMR.

Microwave driven DNP experiments are now recognized as a powerful method of enhancing signals in solid state and solution NMR and imaging. DNP improves the sensitivity of NMR spectra by about a factor of 100, thus reducing the acquisition time in multidimensional NMR experiments by roughly 10^4. This enhancement permits studies of larger molecules, reaction dynamics or high-throughput screening [8].

These early, successful efforts in microwave driven DNP NMR could be extended to magnetic fields of up to about 3.4T using commercially available sources, such as klystrons, at a frequency of up to 94 GHz. However, modern NMR spectroscopy has pushed to much higher magnetic fields, where much better spectral resolution is achieved. The extension of DNP NMR to high magnetic fields had to wait for the development of THz sources of radiation at the relevant frequencies. Fortunately, the development of the THz gyrotron enabled this extension of DNP NMR into the high magnetic field regime.

The first DNP NMR experiments using a gyrotron were conducted by Becerra et al. at the MIT Francis Bitter Magnet Laboratory at a magnetic field of 5 T, corresponding to 211 MHz NMR frequency and 140 GHz microwave frequency [9]. This successful advance was followed at MIT by extension of the technique to 9T with the development of a 250 GHz gyrotron for use in a 380 MHz spectrometer [10] and later extension to 16 T with the development of a 460 GHz gyrotron for a 700 MHz spectrometer [11]. Research on the gyrotron also led to the discovery of broadband tuning of the gyrotron source, which could be useful in partially covering the electron spin resonance spectrum in DNP NMR experiments [11, 12].

Interest in THz DNP NMR has now developed in many laboratories worldwide. A 260 GHz / 400 MHz spectrometer is in operation in Frankfurt, Germany [13, 14] and a 395 GHz / 600 MHz spectrometer is operating at the Osaka Institute in Japan [15]. Instrumentation for a 263 GHz / 400 MHz DNP NMR system has been developed by industry and used in DNP NMR research [14, 16, 17]. As described by Griffin and Prisner in a recent article, DNP NMR is truly enjoying a "renaissance" at the present time [8].

This paper is organized as follows. In Section II, the THz DNP NMR technique is described in detail. Section III

Manuscript received Xxxxx YY, ZZZZ.

E. A. Nanni is with the Department of Electrical Engineering and Computer Science and the Plasma Science and Fusion Center, Massachusetts Institute of Technology, Cambridge, MA 02139 USA (corresponding author, tel. 617-253-2303; fax: 617-253-6078; email: enanni@mit.edu).

A. B. Barnes is with the Department of Chemistry and the Francis Bitter Magnet Laboratory, Massachusetts Institute of Technology, Cambridge, MA 02139 USA (e-mail: barnesab@mit.edu)

R. G. Griffin is with the Department of Chemistry and the Francis Bitter Magnet Laboratory, Massachusetts Institute of Technology, Cambridge, MA 02139 USA (e-mail: rgg@mit.edu)

R.J. Temkin is with the Department of Physics and the Plasma Science and Fusion Center, Massachusetts Institute of Technology, Cambridge, MA 02139, USA (e-mail: temkin@mit.edu).

describes the source technology used in THz DNP NMR. Section IV describes the transmission lines for transporting the radiation from the source to the sample. Section V describes the sample probe, sample holder and the coupling of the THz power into the sample. Section VI is the Summary and Conclusions.

II. THz Dynamic Nuclear Polarization NMR

The structure and function of biomolecules are strongly correlated. Determining three-dimensional structural detail of proteins at an atomic resolution is crucial to understanding how they work as machines, how they catalyze chemical reactions, how they bind to each other, as well as their interaction with drugs and signaling molecules. By far, the most powerful technique available for structure determination is X-ray diffraction. However, there are certain drawbacks of X-ray crystallography; namely, the highly ordered crystalline environment required to record diffraction patterns is not a truly biological environment. In vivo, proteins are in solution, bound to or embedded inside the cellular membrane, intrinsically disordered, or arrange themselves into amyloid fibrillar strands. For such molecules in a biologically realistic environment, X-ray diffraction is not applicable and the magnetic resonance of nuclear and electron spins can be leveraged to determine structural detail. In particular, the site-specific signals of nuclear spins can reveal sub-angstrom level structural detail of proteins and molecules. Due to the excellent resolution of NMR spectra, NMR has evolved as the preferred spectroscopic approach for the solution of problems in many areas of science, including physics, chemistry, biology, materials science, and more recently medicine.

Nevertheless, the sensitivity of NMR experiments is low when compared to other spectroscopic approaches. Furthermore, since both high resolution solid and solution state NMR are utilized with increasing frequency in structural studies of macromolecular biological systems-proteins, nucleic acids, etc.-sensitivity continues to be an issue of paramount importance in the successful application of the technique.

DNP has successfully improved the sensitivity in NMR experiments by factors of 20-400 (corresponding to 400-160,000 in acquisition time) [19, 20], depending on the experimental conditions such as temperature, solvent composition, deuteration levels, radical type and concentration, etc. The increased signal intensity shortens the acquisition time, reduces the amount of sample required and allows the acquisition of multidimensional spectra with high signal to noise. The following subsections illustrate the mechanism of polarization transfer for efficient DNP at high fields and show that large DNP polarization enhancements are consistently obtained at high field. These results demonstrate applications to structural studies of biologically significant systems which would not be feasible without DNP.

A. Mechanisms of DNP

DNP was first proposed and performed in the 50's [2, 3], and in the 80's DNP experiments were incorporated into MAS experiments with a goal of increasing signal intensities in the spectra [6, 7]. MAS of samples in solid-state NMR (SSNMR) spectroscopy reduces line broadening in spectra by spinning at the "magic angle" of 54.7 degrees with respect to the magnetic field, B_0. These initial MAS DNP experiments used 40 GHz microwaves (1.5 T) and the solid effect (SE); signal enhancements of 25 were observed at ~300 K [5, 21-24]. Subsequently, DNP experiments were initiated at MIT at 140 and 250 GHz (5 and 9 T fields) [9, 10, 25-29] using gyrotrons.

The two mechanisms that are most important for continuous wave (CW) DNP processes in MAS experiments are the solid effect (SE) and the cross effect (CE). Which of the two mechanisms dominate (SE or CE) depends on the size of the inhomogeneous breadth, Δ of the electron paramagnetic resonance (EPR) spectrum, compared to the nuclear Larmor frequency, ω_{0I}, and the homogeneous breadth, δ.

The SE is a two spin process (Fig. 1a left) that governs the polarization process when $\omega_{0I} > \Delta,\delta$ and thus requires a

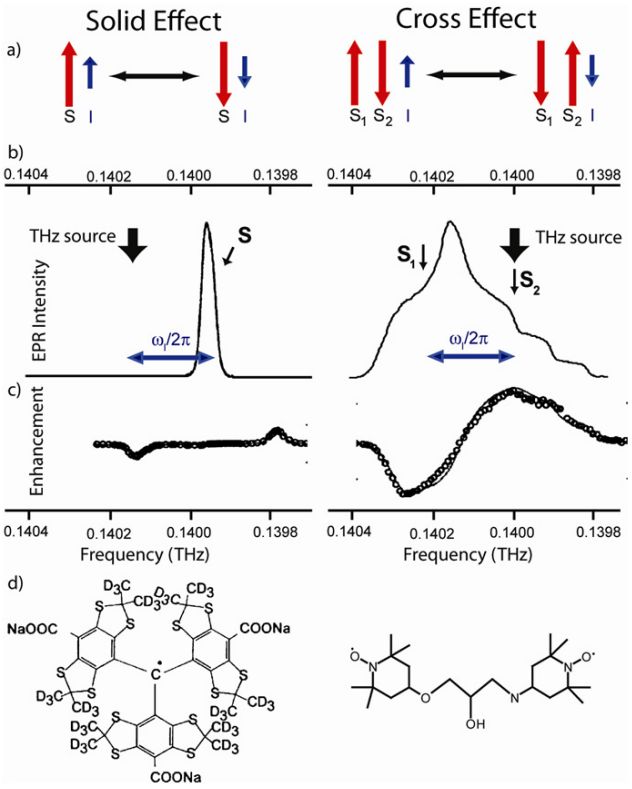

Fig. 1. Common DNP polarization transfer mechanisms in solid dielectrics. a) In the SE, one electron and one nuclear spin flip simultaneously with excitation from THz radiation, whereas the CE involves two electron spins and one nuclear spin. b) EPR spectra of the radicals that are the polarization source in THz DNP experiments. (left) The SE utilizes narrow line radicals such as trityl. (right) EPR spectra of nitroxide radicals such as TEMPO or TOTAPOL are much broader and used for the CE. c) Field/frequency dependent profiles of the two mechanisms. In the SE (left) the THz source is set to ω_{0I} away from the center of the EPR line. (right) For the CE, the THz radiation is on resonance with one of the two electrons involved. d) chemical structures of typical radicals used for the SE; trityl (left) has a mostly isotropic environment around the unpaired electron density which results in a similar resonance frequency (narrow line) across the powder average of the crystallites. TOTAPOL (right) for the CE, more anisotropic chemical environments around the electron density yield broader lines such that two electrons are separated by ω_{0I} and fulfill the matching condition. (Adapted from [18])

radical with a narrow line such as trityl (Fig. 1b, d left). The frequency dependence of the enhancement profile for trityl is illustrated in Fig. 1c (left) and shows minima and maxima when the irradiation frequency is $\omega_{0S}\pm\omega_{0I}$, where forbidden electron-nuclear flip-flops are excited leading to a negative or positive enhancement. Since the SE utilizes forbidden transitions the enhancements scale as ω_0^{-2} and are therefore attenuated at higher fields [30].

The CE, a three spin effect (Fig. 1a, right), is a DNP mechanism that has been shown to yield more efficient transfers at high-field. It relies on the fact that the resonance frequencies of two electrons, ω_{0S1} and ω_{0S2} in the EPR spectrum, satisfy the condition $\omega_{0S1}-\omega_{0S2}=\omega_{0I}$ (Fig. 1b,c right) and as such the enhancements scale as ω_0^{-1}. Furthermore, the CE works well with a large set of radicals such as nitroxides (TEMPO and its relatives), in which $\Delta>\omega_{0I}>\delta$ at high field. Assuming dipole-dipole couplings exist amongst the two electrons and the nucleus, THz irradiation near either ω_{1S} or ω_{2S} flips one of the electrons up, the other down, and the energy difference between the two spins goes into polarizing the nuclear spin.

The efficiency of CE depends on two spatial factors: (1) the distance between the electron spins, which determines the electron-electron dipolar coupling and (2) the relative orientation of the two radicals, which determines, via the g-anisotropy tensors, the frequency separation $\omega_{0S1}-\omega_{0S2}$. For the case of biradical polarizing agents, both of these factors can be optimized by design of the molecular linkage tethering two nitroxide groups such as that found in 1-(TEMPO-4-oxy)-3-(TEMPO-4-amino)propan-2-ol (TOTAPOL) [31] (Fig. 1d, right) and bis-TEMPO-bis-ketal (bTbK) [19]. The magnitude of the maximum enhancement obtained with the water-soluble TOTAPOL radical is ~175 at 212 MHz with 6 W of THz power [31], an improvement by a factor of ~4 from monomeric nitroxides, like TEMPO. Since the tether connecting the two TEMPO groups is relatively flexible, their relative orientation is not tightly constrained and many biradicals do not have the correct geometry corresponding to the desired separation frequency. Therefore, with a more rigid tether that can lock the two TEMPOs at a desired relative orientation, it is possible to further improve the performance of a polarizing agent. Enhancements of 250 with 4 W of THz power are achieved using bTbK, a new biradical connecting two TEMPOs with a rigid bis-ketal tether [19]. Thus, significant gains in enhancements have been realized by optimization of polarizing agents for high-field DNP.

An important point illustrated in Fig. 1c is that magnetic field (B_0) has to be swept to the appropriate point in the EPR spectrum in order to optimize the DNP enhancement. In present day DNP spectrometers, this is accomplished with a superconducting sweep coil that was installed on the magnet at the time it was manufactured. In NMR magnets that lack a sweep coil, a tunable source of THz radiation would be useful, see discussion in Section III.F.

Other spectroscopic techniques are enabled by double resonance (NMR and microwave) methods. The Overhauser effect (OE) [2] is important for conducting solids (metals, etc.) and solution samples. Thermal mixing involves a homogeneously broadened EPR spectrum [32] that is present at low magnetic field and as such is not applicable for THz DNP.

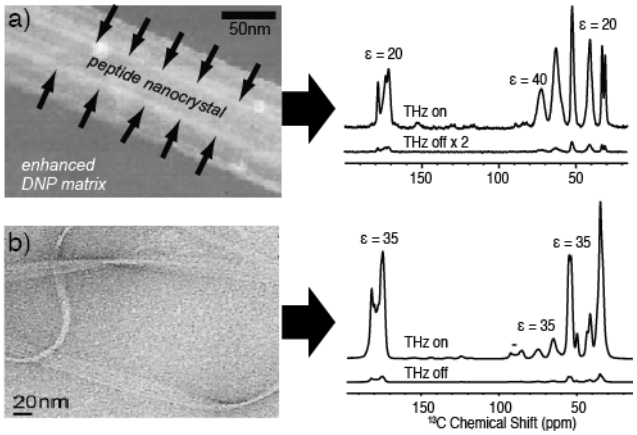

Fig. 2. Electron micrographs and 0.263 THz DNP spectra of GNNQQNY showing a signal enhancement of a) 20 on the nanocrystals and b) 35 on the amyloid fibrils. (Adapted from [33], [34] , and [35])

B. *Applications of THz DNP in Solids*

DNP has been demonstrated to be an extremely versatile technique, resulting in drastic gains in sensitivity in a wide range of biological systems ranging from nanocrystalline peptides [33] and amyloid fibrils [35], to proteins in virus capsids [36] soluble proteins [27], and membrane proteins embedded in lipid bilayers [27]. Similar DNP strategies have recently been extended to materials research and inorganic chemistry applications to enhance signals from nuclear spins on surfaces [37]. This section describes in more detail some of these initial applications of THz DNP.

1) *Amyloid Fibrils and Nanocrystals*

Proteins are chains of amino acids strung together through covalent peptide linkages. After synthesis, they must fold into the correct three-dimensional structure to perform their biological function. Proteins that miss-fold can aggregate and cause numerous diseases such as Alzheimer's and cystic fibrosis [38, 39]. DNP NMR is well suited to determine the atomic resolution structure of these pathogenic aggregates [40], sometimes referred to as amyloid fibrils or prions. Understanding the structure can yield insight into how and why they form and in turn help combat the associated diseases.

$GNNQQNY_{7\text{-}13}$ (where each letter stands for a single peptide) is a polypeptide originating from the yeast prion protein Sup35p that can form either nanocrystals or amyloid fibrils. At 212 MHz ^{1}H frequency and 90 K, 0.140 THz DNP yields a substantial enhancement factor of 120 on nanocrystals of GNNQQNY, permitting the acquisition of 2D spectra in only 20 minutes due to the excellent sensitivity available with DNP [33]. The biradical polarizing agent**,** TOTAPOL, is too large to penetrate into the nanocrystals, yet leads to ^{13}C and ^{15}N spectra with enhancements of 120 for the peptide resonances and 160 for the solvent, illustrating that ^{1}H spin diffusion effectively distributes the enhanced polarization throughout the lattice. These initial experiments have been extended to higher fields in a study using a 263 GHz commercial Bruker spectrometer [16] which demonstrated an

enhancement of 20 on nanocrystals (Fig. 2a) and 35 on amyloid fibrils of GNNQQNY (Fig. 2b). This drastic gain in sensitivity may be used for structural determinations of GNNQQNY and other fibrils.

2) Membrane Proteins

Bacteriorhodopsin (bR) is a membrane protein which functions as a light-activated H^+ pump. A retinal chromophore in the center of the protein that is at equilibrium between two conformations (Fig. 3b) absorbs a photon of light that initiates a photocycle consisting of distinct intermediates (Fig. 3a). Despite the fact that there are now ~70 crystal structures available for this protein, the mechanism for its function as a pump is not yet established. The X-ray structures have thus far been unable to resolve essential structural details such as torsion angles in the retinal chromophore in the photocycle intermediates [44] and to decide if the protein is an H^+ pump (as assumed for 30 years) or a backward directed OH^- pump.

SSNMR structural methods are capable of measuring torsion angles and internuclear distances with high precision, but the relative insensitivity of traditional SSNMR is a severe limitation with large proteins. Recording a single 2D data set on a protein with a large effective molecular weight of 32 kiloDaltons typically requires 10 days of signal averaging. However, with DNP enhancements even as low as ε=20, it can be done in less than an hour. This in turn permits the measurement of a variety of torsion angles and distances in the resting state and in photointermediates that will elucidate the pumping mechanism of this protein. Accordingly, experiments confirm that DNP is capable of enhancing the NMR signals in the active site deeply buried in bR by a factor of 50 [45]. Fig. 3c,d shows 2D correlation spectra of a sample which has specific labels at the C14 and Cε position in the active site (yellow box of Fig. 3b). With THz DNP in only 7 hours it is possible to record a spectrum showing correlation peaks between the C14 and Cε carbons [41]. With the sensitivity boost from THz DNP, it was possible to record multiple correlation spectra in which the polarization transfer time between the two carbon sites was varied. The dipolar coupling strength, which is directly related to the distance between the two spins, can then be extracted by the build-up profiles of the correlation peak intensity (Fig. 3d). In addition to these experiments that measured inter-nuclear distances to sub-angstrom precision, THz DNP also revealed heterogeneity in the different conformational states of bacteriorhodopsin [43].

In the resting state of the protein, what was previously thought to be only one conformer, bR_{555} clearly is resolved as two resonances in the 2D spectrum (Fig. 3e, left). Furthermore, the L intermediate (blue box of Fig. 3a) was shown to actually consist of four states (Fig. 3e, right), three of which are shunt states that do not result in a proton being pumped across the membrane [43].

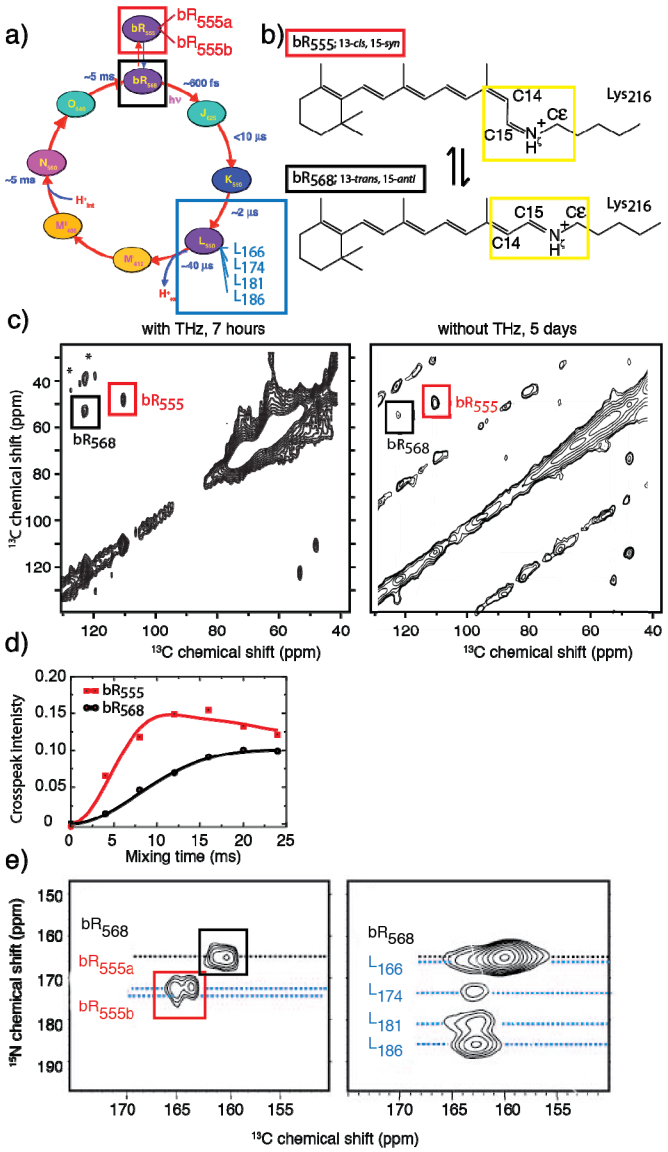

Fig. 3. a) Photocycle illustrating the intermediates examined with DNP enhanced MAS spectra. b) The conformational equilibrium of the retinal chromophore in the resting state. The yellow box highlights the nuclei in the spectra in the lower panels. c) 2D spectra of the active site of bR showing correlation peaks between C14 and Cε recorded in 7 hours with THz DNP and 5 days without THz DNP even with 10 times more sample. d) build-up profiles of the correlation between C14 and Cε. The profiles are fit and yield a distance of 3.11±0.22 Å between the C14 and Cε in bR_{555} and 3.90±0.08 Å in the bR_{568} trans conformation. e) $^{15}N\zeta$-$^{13}C15$ correlation experiments provide assignments of the retinal-C15 resonance in each state: (left) the dark-adapted state; (right) the mixture of L intermediates. (Adapted from [41], [42] and [43])

C. DNP for Solution State NMR

There is considerable interest in applying DNP techniques to high field solution NMR experiments. Recently, significant progress has been made in performing DNP directly in the solution state using a 263 GHz gyrotron [13]. However, it is also possible to perform a polarization step and melting *in situ*, the latter being performed with CO_2 laser radiation. This experiment is referred to as *in situ* temperature jump DNP (TJ-DNP) [20].

A schematic representation of the TJ-DNP cycle is shown in Fig. 4. In the experiment, the DNP NMR probe was maintained at 90 K, and the frozen sample was polarized with microwave irradiation at 140 GHz. Polarization was then transferred by cross polarization from ^1H to ^{13}C. The sample was then rapidly melted by a CO_2 laser pulse (10 W for 1.2s, λ=10.6 µm), and a ^{13}C solution NMR signal was immediately recorded with ^1H decoupling. Fig. 4b shows the solution spectrum (right) as well as the SSNMR ^{13}C spectrum obtained

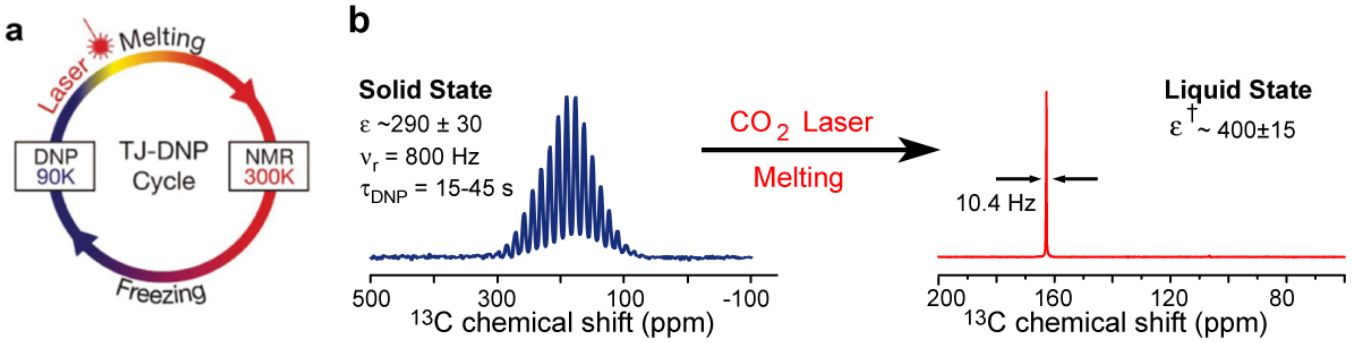

Fig. 4. a) Conceptual representation of the TJ-DNP experiment showing the four stages associated with acquisition of a DNP enhanced liquid state spectrum. b) MAS spectrum produced at 90 K, ε ~ 290 from a urea sample and the resulting liquid state spectrum with an enhancement ε† ~ 400. (Adapted from [20])

with DNP but without melting. For this sample (^{13}C-urea in DMSO/water), the sensitivity enhancement that was observed was 400±15 relative to the normal solution NMR experiment carried out entirely at room temperature [20]. Fig. 4 shows a spectrum in which TJDNP is integrated into a 2D ^{13}C-^{13}C experiment.

III. Gyrotrons for DNP NMR

A. THz Sources

As DNP NMR experiments move to higher magnetic fields, several requirements make gyrotrons the most practical source for THz radiation. As seen in Table I, the THz source must be capable of producing a minimum of 10 W CW, while providing frequency and power stability for the duration of NMR signal acquisition period (≥ 36 hours). Additionally, the life time of the device must also be considered, due to the major capital and personnel investments involved in NMR research.

Table I

Requirements for DNP NMR Gyrotrons	
Frequency	~28 *B_0 GHz (B_0 = NMR field in T)
Output Power	>10 W
Power Stability	1 %
Frequency Stability	10 MHz
Run Time	>36 Hours
Lifetime	>50,000 Hours

The generation of millimeter, sub-millimeter and THz radiation at high power has proved to be a significant challenge. In Fig. 5, updated from the review article [46], the state of the art capabilities for solid state and vacuum electron sources is shown. As seen in Fig. 5, solid state devices in the THz range suffer from scalability and efficiency issues, that lead to limited output powers. However, they have proved useful in some DNP NMR experiments that use small sample sizes and metallic resonators [6, 47-49] suitable for aqueous and static (non-MAS) DNP experiments. Classical microwave tubes, e.g. klystrons and traveling wave tubes, can produce high power (hundreds of Watts) electromagnetic radiation up to 100 GHz, but these slow wave devices require physical structures in the interaction cavity that are much smaller than the wavelength of operation. This small element size produces difficulties with thermal damage and manufacturing of the interaction cavity when the frequency is extended into the THz range. Furthermore, at THz frequencies slow wave devices suffer from reduced lifetime due to electron beam interception and high heat loads. The Extended Interaction Klystron (EIK) is a possible source for THz radiation needed in DNP experiments. As an oscillator it has achieved an average output power of 7 W at 220 GHz, and an average output power of 0.3 W at 280 GHz [50, 51]. The EIK is promising for DNP applications, but has limited power and may have limited lifetime at THz frequencies.

Electron cyclotron resonance masers (gyrotrons) are capable of producing high average power in the microwave, millimeter wave and THz bands [52]. Due to the overmoded cavities used in gyrotrons, they remain the only demonstrated, highly stable device capable of producing adequate power levels (a minimum of 10 W CW) with an adequate lifetime (about 100,000 hours), in the frequency range of interest for DNP NMR.

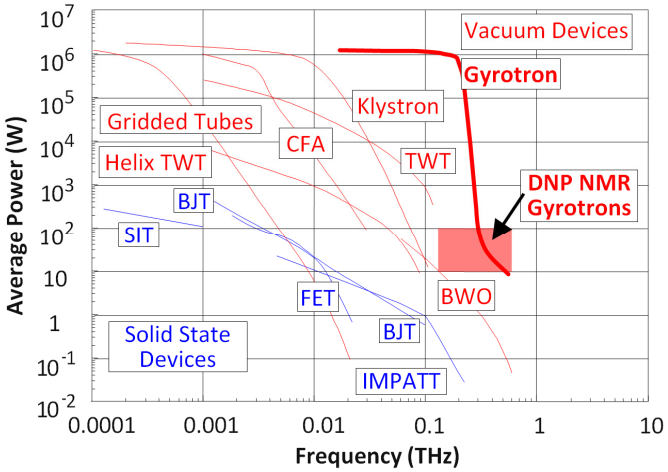

Fig. 5. State-of-the-art of solid state and vacuum electron devices. (Adapted from[46])

B. Fundamentals of Gyrotrons

In gyrotrons the emission of coherent THz radiation results from the resonant interaction between the eigenmodes of a cavity, typically cylindrical, and a mildly relativistic electron beam that is gyrating in a constant axial magnetic field. The basic configuration of a gyrotron, Fig. 6, consists of a magnetron injection gun (MIG) that launches an annular electron beam into the hollow bore of a solenoidal magnet.

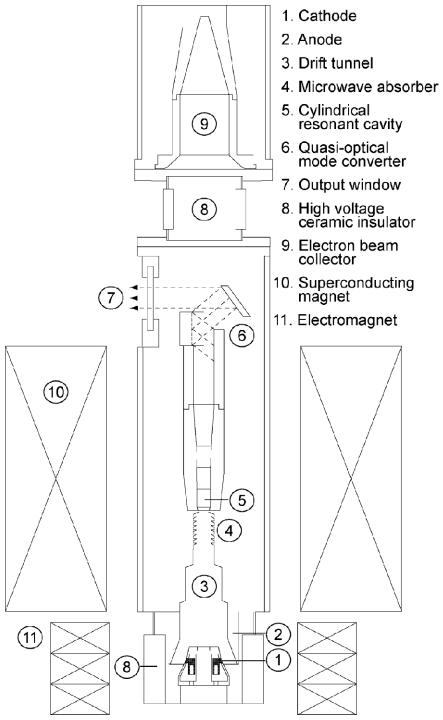

Fig. 6. Cross-sectional schematic of a typical cylindrically symmetric gyrotron tube used in DNP NMR experiments, not shown to scale, indicating key components. (Adapted from [11])

The magnetron injection gun is located at the bottom of Fig. 6. The axial magnetic field is produced by a DC superconducting magnet. A second magnet can be added at the location of the MIG to provide additional control of the electron beam compression and velocity ratio. In the MIG, the orientation of the DC electric field that extracts the electron beam from the cathode produces a beam that has both a perpendicular and parallel velocity component with respect to the axial field produced by the solenoidal magnet. As the electron beam travels into the central bore, it undergoes adiabatic compression that increases its orbital momentum. The electrons enter a metallic cavity that has an eigenmode resonance that is close in frequency to a harmonic of the gyration frequency of the electron. The electron beam surrenders some of its kinetic energy to the electromagnetic mode through stimulated emission. The electrons exit the cavity and are deposited on a metallic collector. The gyrotron resonator supports a high order cavity mode that is difficult to transport over long distances. It is often convenient to convert the wave into a Gaussian beam that can be efficiently extracted in a transverse direction using mirrors.

In order for the electron beam to interact with the electromagnetic mode in the cavity, a harmonic of the relativistic electron frequency must be close to the frequency of oscillation for the cavity mode [53]. The relativistic cyclotron frequency is

$$\Omega_c = eB_0/\gamma m_e \quad (1)$$

where e is the charge of the electron, B_0 is the DC axial magnetic field, m_e is the electron mass and γ is the Lorentz factor $(1-v^2/c^2)^{-1/2}$, where v is the velocity of the electron, c the speed of light. In a cylindrical cavity, of radius r_w and length L, the dispersion relation for TE modes is

$$k^2 - k_\perp^2 - k_z^2 = 0 \quad (2)$$

where $k = \omega/c$ is the wave vector in free space, ω is the frequency of the THz wave, $k_\perp = \nu_{mn}/r_w$ is the transverse propagation constant, ν_{mn} is a root of the Bessel function $J'_m(x)$ and k_z is the axial propagation constant (approximately $q\pi/L$, where q is an integer). The cyclotron beam mode dispersion relation is

$$\omega - k_z v_z - s\Omega_c = 0 \quad (3)$$

where v_z is the axial velocity of the electrons and s is the integer cyclotron harmonic number. When the frequency of the mode and the resonance intersect, as seen in Fig. 7, oscillation and stimulated emission can occur. The dotted/dashed line and the dashed line in Fig. 7 are the cyclotron beam mode dispersion relation or Doppler shifted resonance condition for $s = 1$ and $s = 2$, respectively. The black circle is a fundamental forward wave oscillation, the square is a second harmonic forward wave oscillation and the diamond is a fundamental backward wave (BW) oscillation. Traditionally, gyrotrons interact with the fundamental forward wave [9, 10, 16], however the second harmonic forward wave is useful for higher frequency experiments [11, 12, 54, 55] and the BW interaction is used at the first or second harmonic to provide the frequency tunability in gyrotrons for DNP NMR experiments.

The cavity in a gyrotron typically consists of a central cylindrical region, with a down taper on the gun side and an uptaper on the collector side. A cross section of cavity is shown in Fig. 8. Superimposed over the cavity is the axial electric field profile for the mode of the cavity shown, which is a $TE_{4,3,1}$ mode. The interaction between electron beam and the cavity mode occurs only at the radius of the annular electron beam, r_e, as shown in the insert of Fig. 8. Because the cavity modes are non-uniform in the radial direction, the

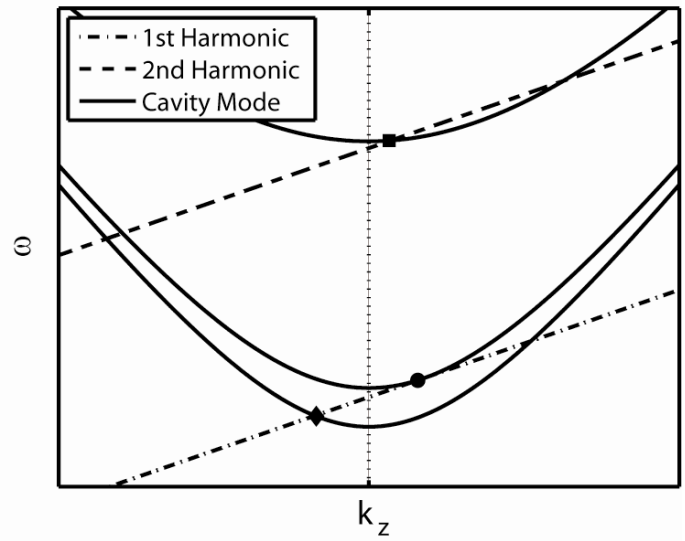

Fig. 7. Dispersion diagram for the Doppler shifted cyclotron resonance and cylindrical cavity modes.

strength of the interaction between the beam and a cavity mode is determined by the radial placement of the electron beam. This can be advantageous (especially in second harmonic experiments) by allowing for the selection of a desired mode.

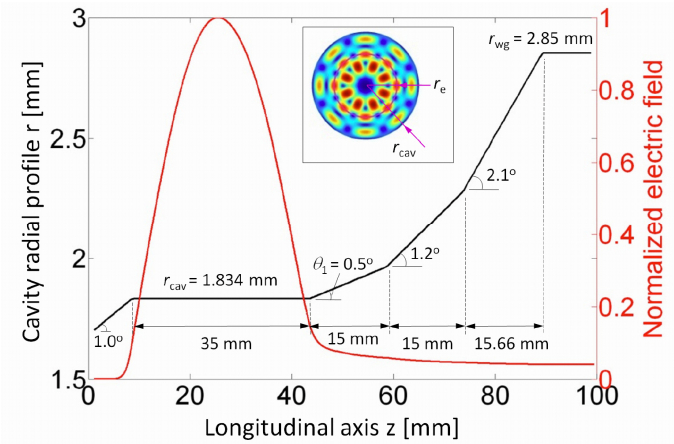

Fig. 8. Geometrical profile of a cylindrically symmetric 330 GHz gyrotron cavity and the electric field profile of the excited $TE_{4,3,1}$ mode. The insert shows the transverse electric field profile of the cavity mode. The electron beam radius is labeled as r_e. (Adapted from [56])

C. *Nonlinear Theory of Gyrotrons*

For an exact understanding of the operation of a gyrotron oscillator, the interaction between an energetic electron and the electromagnetic mode confined in the resonator or interaction cavity must be described. In a gyrotron, kinetic energy is extracted from the electron beam as it passes through the interaction cavity. However, a gyrotron does not extract any energy from the axial component of the velocity, only from the transverse component. This energy extraction is made possible because an electron traveling in a circular path around a DC magnetic field will feel an accelerating or decelerating force from the resonant oscillating electric field that can deposit or extract energy from the electron. The initial applied force from the cavity mode results in some electrons gaining energy and some electrons losing energy. The more energetic electrons to rotate slower and the less energetic electrons to rotate faster, because of the dependence of γ and Ω_c on velocity and energy. The different rotational frequencies produce phase bunched electrons that act coherently to deposit energy into the electromagnetic mode of the cavity. This process can be described by the pendulum equations that relate the change in energy and momentum for the electron to the electric and magnetic fields that are present. The equations of motion for the electron are

$$\frac{\partial \mathcal{E}}{\partial t} = -e\mathbf{v}\cdot\boldsymbol{E} \tag{4}$$

$$\frac{\partial \boldsymbol{p}}{\partial t} = -e(\boldsymbol{E} + \mathbf{v}\times\boldsymbol{B}) \tag{5}$$

where the electron energy is $\mathcal{E}$, the momentum $\boldsymbol{p}$, the THz electric field is $\boldsymbol{E}$, the DC magnetic field is $\boldsymbol{B}$ and the velocity of the electron is $\mathbf{v}$. The instantaneous kinetic energy and momentum of a relativistic electron are $\mathcal{E} = \gamma m_e c^2$ and $|\boldsymbol{p}| = \gamma\beta m_e c$ respectively, where $\gamma = (1 - \beta^2{}_\perp - \beta^2{}_z)^{-1/2}$ and $\beta = \mathrm{v}/c$.

It is useful to convert these equations into normalized variables for the practical case of a cylindrical resonator by taking into account the strength of the coupling between the electron and electromagnetic mode. The conversion to the normalized pendulum equations is covered in detail by [53, 57] and results in

$$\frac{\partial u}{\partial \zeta} = 2Ff(\zeta)(1-u)^{n/2}\sin\theta, \tag{6}$$

$$\frac{\partial \theta}{\partial \zeta} = \Delta - u - nFf(\zeta)(1-u)^{\left(\frac{n}{2}-1\right)}\cos\theta. \tag{7}$$

where the normalized variables are the electron energy u, the electron phase θ, the axial position ζ, the field strength F, the cavity length μ and the magnetic field detuning Δ. With a cavity length L and assuming a Gaussian axial field profile

$$f(\zeta) = e^{-(2\zeta/\mu)^2}, \tag{8}$$

$$\mu \equiv \pi\frac{\beta_\perp^2}{\beta_z^2}\frac{L}{\lambda}. \tag{9}$$

The beam-wave coupling has been incorporated into F [57]. These coupled differential nonlinear equations of motion describe a gyrating electron interacting with an electromagnetic field, by tracking the normalized transfer of energy and the phase of the electron. Equations (6) and (7) are only functions of three parameters: F, μ and Δ. In a gyrotron an electronic efficiency of up to 70% is achievable with the optimization of these parameters [57].

D. *Development of THz Gyrotrons*

The discovery of the cyclotron resonance instability by R. Twiss [45], J. Schneider [58] and A. Gapanov [59] was followed by the first detailed experimental demonstration by Hirshfield and Wachtel [60]. The first high power gyrotron in the THz band produced a kilowatt of power at a frequency near 300 GHz [17]. Pulsed THz gyrotron oscillators with several hundred kW of power were also developed [61-63], reaching almost 1 MW of power at 300 GHz [64]. In the past two decades, progress has been made on providing useful millimeter and sub-millimeter wave sources for Electron Cyclotron Resonance Heating (ECRH) of plasmas [52, 56]. At very low power levels, step tunable gyrotrons have been demonstrated at frequencies in the THz band for spectroscopy [65-67]. Gyrotrons were developed at power levels of 10 to 100 watts for application to DNP NMR and EPR experiments [9-12, 16, 54, 55]. The gyrotrons for DNP NMR must meet exacting specifications for reliability, efficient power conversion, frequency bandwidth and signal stability. With interest in developing this technology for higher frequency NMR experiments, these THz sources present a challenge to THz technology for sources, transmission lines and related components. A comprehensive review of the history and present state of THz vacuum electronics is provided in this journal issue [68].

E. DNP Experiments with Gyrotrons

In 1992 the first use of a gyrotron for a DNP NMR experiment was reported by Becerra et al. [9] using a 140 GHz CW gyrotron capable of producing 20 W. Signal enhancements for polystyrene doped with BDPA of 10 for ^{1}H and 40 for ^{13}C were reported when comparing NMR spectra recorded with and without microwave power. The 140 GHz gyrotron operated in the TE_{031} mode of a cylindrical resonator with a 42 kV, 10-100 mA electron beam producing 20 W CW and 200 W pulsed. This was the first gyrotron with enough stability for phase-coherent magnetic-resonance spectroscopy. The power is converted internally to the TE_{01} mode and extracted from the gyrotron after a miter bend through a window. A transmission line and mode converters provide the power to a WR-8 waveguide that goes to the sample and radiates the power along the axis of rotation of the MAS sample. Recently, the gyrotron was upgraded to be operated with a lower voltage MIG [26, 69] with the key parameters of the 140 GHz gyrotron listed in Table II. A photo of the system is shown in Fig. 9. The bandwidth of the gyrotron has been measured using a heterodyne receiver system. The emission bandwidth of the gyrotron was found to be 1 MHz at 60 dB below the carrier [70, 71]. This is the most sensitive measurement to date of noise in a gyrotron and the results assure that parasitic modes do not participate in the excitation of the electron spins in DNP NMR spectroscopy. This gyrotron has remained in service for nearly two decades of operation.

Table II

140 GHz Gyrotron Parameters	
Operating Mode	TE_{031}
Voltage	12 kV
Current	35 mA
Beam radius	1.82 mm
Output Power	15 W
Magnetic field	5.12 T
Beam Velocity ratio	1.6

A 250 GHz DNP NMR system [10, 72] was commissioned at MIT in 2000 with a design that improved upon the 140 GHz spectrometer. This gyrotron produces 15 W with a 12 kV, 35 mA electron beam in the TE_{032} mode. ^{1}H Enhancements of up to 170 have been observed for 1-^{13}C-glycine at temperatures of 20 K using a MAS probe [10]. The gyrotron, transmission line and NMR setup are shown in Fig. 10. The 250 GHz gyrotron is designed to operate in a vertical orientation in order to simplify support and alignment. A radial bore in the magnet allows the transmission of the microwave power through a side vacuum window of the tube. As a result, the electron beam and microwave power can be separated just after the interaction in the gyrotron cavity. An internal Gaussian beam mode converter was included in the design. This reduces ohmic losses in the output waveguide and simplifies the design of the beam collector and microwave transmission line. A specially built corrugated transmission line with very low loss brings the power from the gyrotron to the sample [73]. The transmitted beam had a measured Gaussian beam content of 93% [74]. The gyrotron output power is monitored and controlled by feedback stabilization.

Fig. 9. 140 GHz Gyrotron Oscillator (right), control system (left), grad student Mr. Andrew Casey.

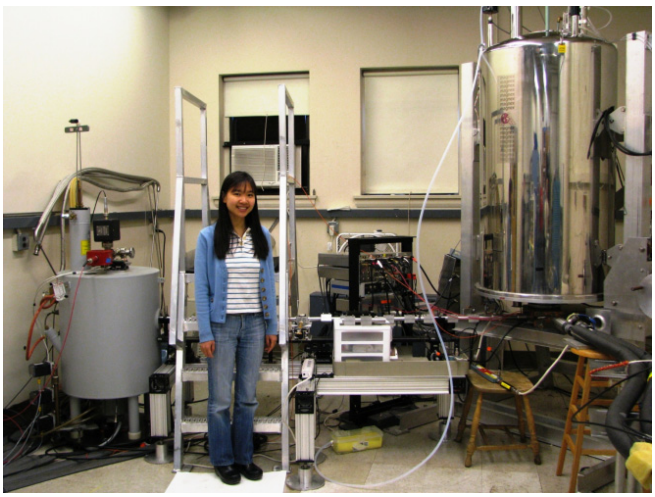

Fig. 10. Photo of the 250 GHz gyrotron oscillator (left), the 380 MHz NMR spectrometer (right) and Ms. Melody Mak-Jurkauskas, a graduate student.

In recent years, gyrotrons have been built for DNP NMR research by several groups throughout the world. The first commercial DNP system using a gyrotron is a 263 GHz/400 MHz NMR spectrometer that was developed in 2009 by Bruker BioSpin [16], shown in Figs. 11 and 12.

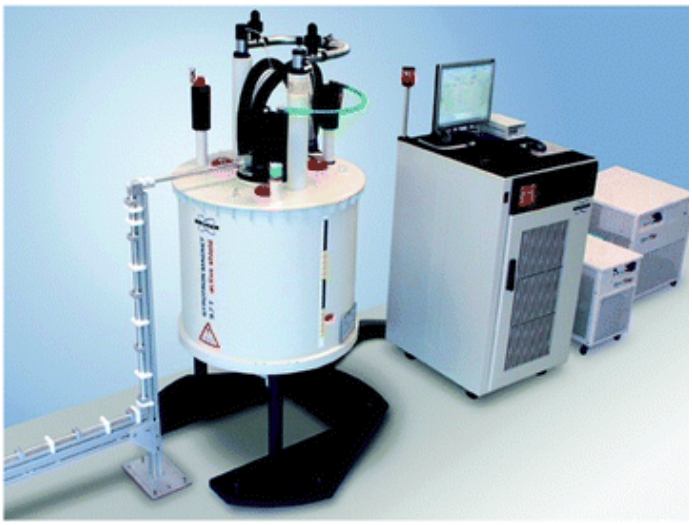

Fig. 11: Commercial DNP/NMR spectrometer with the gyrotron and magnet shown at the left and the control and cooling systems for the gyrotron shown on the right. (Adapted from [16])

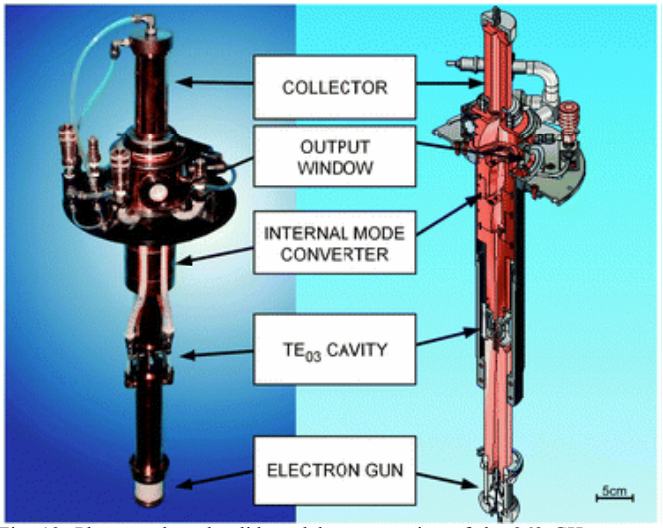

Fig. 12. Photograph and solid model cross section of the 263 GHz gyrotron tube used in the spectrometer of Fig. 7. (Adapted from [16])

More recently, gyrotrons that operate at the second harmonic of the electron cyclotron frequency ($\omega \approx 2\Omega_c$) have been developed for DNP NMR experiments due to the reduced requirements placed on the magnetic field of the gyrotron (half the magnetic field required for fundamental operation). Unique physics and engineering challenges arise at the second harmonic due to reduced efficiency and fundamental mode competition. These difficulties were overcome by careful design of the resonator and choice of the operating mode which is relatively isolated in the mode spectrum. The first completed second harmonic gyrotron for DNP NMR applications was a 10 W, 460 GHz gyrotron oscillator for NMR at 700 MHz [11, 12, 70, 75]. The electron beam parameters during operation are a voltage of 12 kV, current of 140 mA, with a beam radius of 1.03 mm. The gyrotron is shown in Fig. 13**.**

With the completion of two additional second harmonic sources in 2009 [54, 55] the first DNP enhancements using second harmonic gyrotrons were reported in 2010 at 260 GHz [13] and 395 GHz [15]. The 260 GHz experiment utilized a 20 W gyrotron and was able to produce signal enhancements of -79 [76] on an aqueous solution of Fremy's salt, far exceeding previous results using a solid state source [13, 49]. The 395 GHz gyrotron is capable of producing 40 W using the TE_{06} mode of a cylindrical cavity with an enhancement of 10 for 1 M $^{13}C_6$-glucose and 10 mM TOTAPOL [15]. A second harmonic gyrotron for DNP has also been built at 330 GHz [12].

F. Tunability

Due to the extremely sensitive frequency requirements of DNP, either a NMR magnet equipped with sweep coils or a THz source that is continuously tunable can be very valuable. Fabricating a gyrotron cavity to operate at a predetermined frequency with $\Delta f_{set} \approx 50$ MHz accuracy would be a major engineering requirement due to the extremely tight tolerance placed on the cavity radius, as can be seen from (2). It is also difficult and expensive to alter the magnetic field of the NMR experiment to match the gyrotron with such accuracy. With a tunable source that is able to vary the frequency over a range much greater than Δf_{set} this engineering challenge is alleviated. The frequency of the THz radiation must agree with electron precession frequency in order to saturate the polarization of the electron spins and provide a signal enhancement. If the frequency is not correct a drastic change in enhancement will be observed, as seen in Fig. 1c. Furthermore, sweeping the frequency over the entire range of the EPR spectrum is of the interest to the user. In general the width of the EPR spectrum grows linearly with the magnetic field of the NMR experiment adding an additional challenge to higher frequency (typically second harmonic) sources.

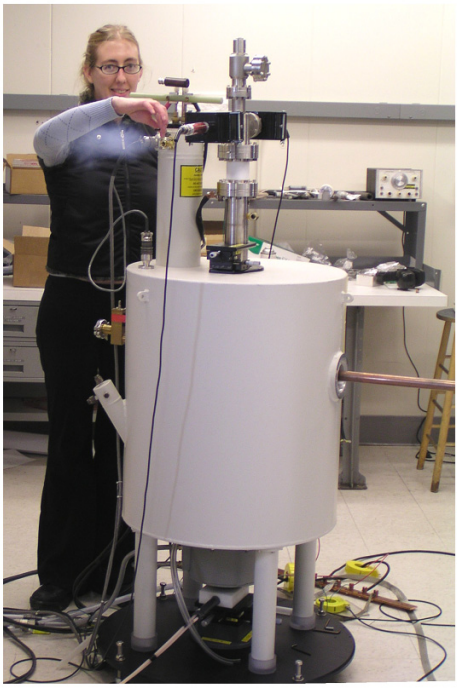

Fig. 13. 460 GHz gyrotron in the superconducting magnet being adjusted by Ms. Melissa Hornstein at MIT. (Adapted from [11])

Continuous tunability in gyrotrons with TE_{mnq} cavity modes can be achieved by keeping the transverse mode numbers (m,n) constant and varying the axial mode number (q). By keeping the transverse index the same, nearly continuous tuning can be achieved by either voltage or magnetic field tuning without affecting the mode converter and transmission line performance. Tuning is improved by increasing the cavity length resulting in a decreased frequency shift from adjacent axial modes via their hybridization. Continuous tunability in a gyrotron for DNP was first reported by Hornstein et al. [11]. In this gyrotron the increased cavity length to lower the oscillation start current for the desired second harmonic mode, led to the hybridization of axial modes, with 2 GHz of tuning reported for fundamental modes near 230 GHz and 50 MHz for the second harmonic mode at 460 GHz, as seen in Fig. 14. When the 460 GHz gyrotron was later rebuilt to operate in the $TE_{11,2}$ mode, over 700 MHz of tuning was observed at the second harmonic [12].

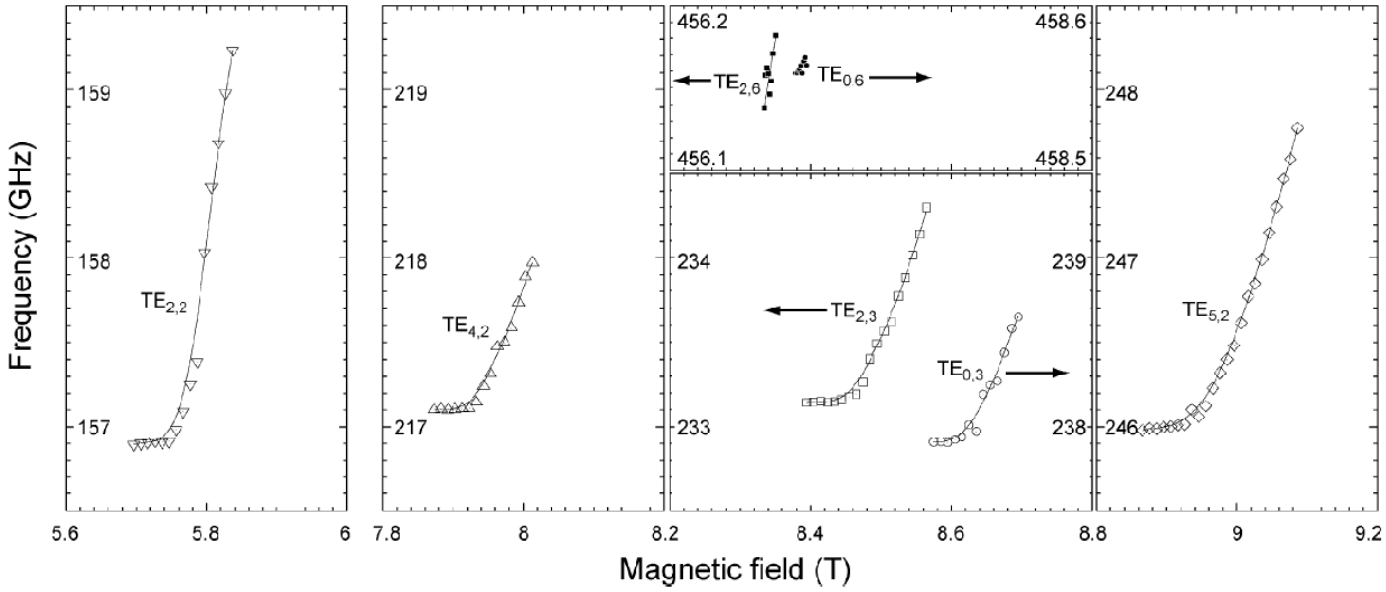

Fig. 14. First observation of continuous tuning in a NMR DNP gyrotron. (Adapted from [11])

This technique for achieving continuous tuning has also been implemented in a 330 GHz second harmonic oscillator [56]. A continuous tuning range of 1.2 GHz was observed experimentally via a combination of magnetic, voltage and thermal tuning. Thermal tuning is achieved by the precise control of the cavity cooling, allowing the cavity to expand or contract as needed. An additional advantage to long cavities is that the start current for oscillations is lowered for all axial modes allowing for operation with smaller beam powers. For a beam voltage of 10.1 kV the oscillation start current for the 330 GHz gyrotron is shown in Fig. 15.

Tuning of over 1 GHz has recently been achieved in a 395 GHz gyrotron [55, 77]. The 1.6 GHz of tuning shown in Fig. 16 demonstrates how switching axial mode numbers (labeled as l in the figure) allows for nearly continuous tuning with magnetic field even with fundamental mode experiments at very high frequencies. On the left side of Fig. 16 the gyrotron is interacting with a forward wave and on the right side of the figure a backward wave.

G. *Internal mode converters*

Extracting THz radiation efficiently from gyrotrons in a manner useful for DNP NMR spectroscopy is very challenging. Internal mode converters that provide high quality Gaussian beams provide the most utility due to the attractive qualities that Gaussian beams provide with respect to transmission, as discussed in Section 4. Internal mode converters are a topic of great interest in the gyrotron community at large due to their power extraction efficiency. Internal mode converters in the form of step cut launchers for azimuthally symmetric modes and helical cut launchers for rotating modes were pioneered by Vlasov [78]. Modern mode converters include the use of quasi-parabolic mirrors to correct for the ellipticity of the beam produced by the launcher. Designs are also optimized using numerical codes, such as the electric field integral equation code Surf3d [79]. One example of an internal mode converter is shown in Fig. 6, labeled as item 6, and in Fig. 17a. This mode converter was designed for use with a $TE_{11,2}$ mode at 460 GHz [80] with a helical cut launcher, parabolic mirror and two flat mirrors shown in Fig.

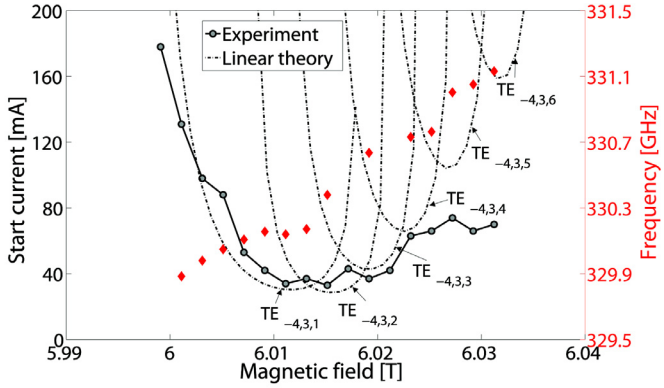

Fig. 15. Measured start oscillation current (solid line) and measured frequency (diamonds) of the operating mode $TE_{-4,3}$ as a function of magnetic field. The theoretical start currents for the first six axial modes $TE_{-4,3,q}$, where q = 1, 2, 3, 4, 5, 6, are shown as dash-dotted lines and they were computed using linear theory. (Adapted from [56])

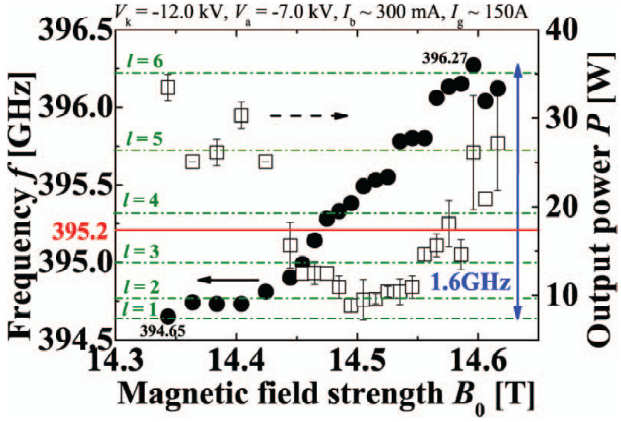

Fig. 16. Tuning with magnetic field from a 395 GHz fundamental mode gyrotron. (Adapted from [77])

17a. The profile of the gyrotron output beam measured with a Spiricon Pyrocam III pyroelectric camera is shown in Fig. 17b. The resulting beam is 92% Gaussian with a waist of w_x = 4.1 mm and w_y = 4.6 mm. Similar mode converters have now been implemented on most DNP gyrotrons [10-12, 16, 54].

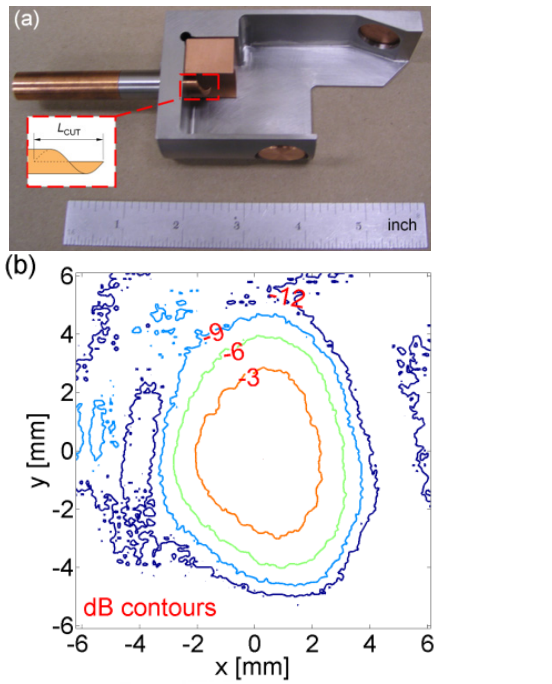

Fig. 17. (a) Quasi-optical mode converter picture with inset showing the helical launcher orientation; (b) measured profile of the mode-converted $TE_{11,2}$ output beam at the window plane at 460 GHz. (Adapted from [80])

IV. Transmission Lines

The power generated by the THz source (gyrotron) must be transmitted to the sample with low loss. In the THz band, it is not possible to use conventional single mode rectangular waveguide for transmission, since the ohmic loss in such guides is much too large. The location of the source, typically a few meters from the NMR spectrometer, requires that the loss per meter be kept as low as possible. Transmission lines for terahertz radiation are an area of intensive research at the present time [81]. Since the frequency bandwidth needed for DNP NMR systems is usually very small, the transmission line can be optimized for a single frequency, thus simplifying the problem significantly. The number of approaches to the design of the transmission line is quite extensive. Free space beaming techniques rely on propagation of a Gaussian-like beam via a series of mirrors and/or lenses. This approach has low loss but may have issues of safety and the stability of alignment. The most common approach is the use of overmoded waveguides, in which the guide radius is much larger than the wavelength. Such waveguides can be corrugated metallic waveguides; dielectric waveguides or dielectric lined metallic waveguides. Reviews of the properties of overmoded waveguides are given by Bhartia and Bahl [82] and Thumm and Kasparek [83].

Fig. 18 shows a schematic of a corrugated metallic waveguide. The guide has grooves of depth d that are one quarter wavelength. The radius a is much larger than a wavelength. Fig. 19 shows the transmission line used in the MIT 250 GHz DNP NMR system [73] and Fig. 20 is a photo of the same system. Fig. 19 illustrates some of the key features of a low loss transmission line. The main transmission line is a 22 mm diameter (a = 11 mm) metallic corrugated waveguide

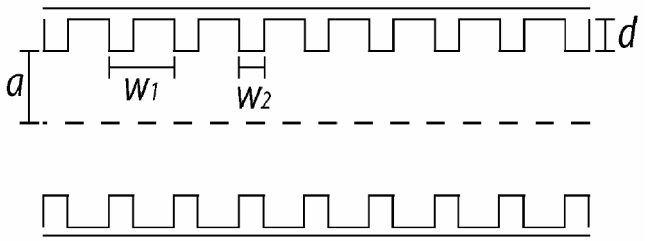

Fig. 18. Illustration of corrugated metallic waveguide of radius a, groove depth d, pitch w_1 and tooth width w_2.

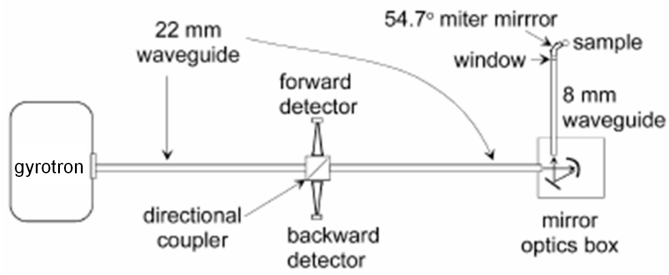

Fig. 19. Schematic of the transmission line used in the MIT 250 GHz DNP NMR system from ref. [73].

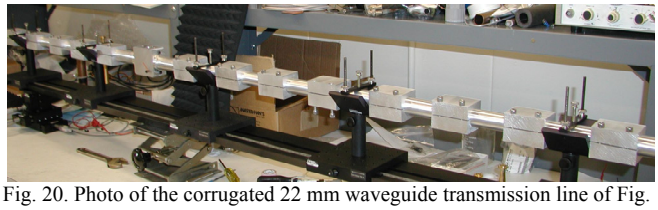

Fig. 20. Photo of the corrugated 22 mm waveguide transmission line of Fig. 18.

made of aluminum. The corrugations d are one quarter wavelength in depth (0.3 mm), one quarter wavelength wide (w_2 = 0.3 mm) with a period of w_1 = 0.4 mm. Two 0.254 m waveguide sections, fifteen 0.124 m waveguide sections and one 0.064 m directional coupler block were assembled with outer diameter clamps to achieve the desired waveguide length.

The modes and ohmic loss in a corrugated waveguide have been developed using the theory of Doane [84]. The linearly polarized output of the gyrotron excites a linearly polarized mode (or modes) in the waveguide [85]. The lowest order mode is the hybrid mode HE_{11}, whose transverse electric field is given by:

$$E^{\perp}(r,\varphi) = (X_{01}/a)J_0(X_{01}r/a) \tag{10}$$

where X_{01} is 2.405 and J_0 is the zero order Bessel function. This expression is valid when the corrugation depth is approximately one quarter wavelength and the radius a is much larger than the wavelength.

The estimated ohmic loss in the overmoded waveguide of Fig. 20 is less than 10^{-3} dB per meter and is thus negligible. The measured loss for the 22 mm diameter waveguide portion of the transmission line of Fig. 20 is shown as open circles in Fig. 21 and amounts to less than 1% per meter.

For perfect excitation of the HE_{11} mode on the transmission line, the overall transmission line loss is expected to be dominated by loss at miter bends and by tilts and offsets in the

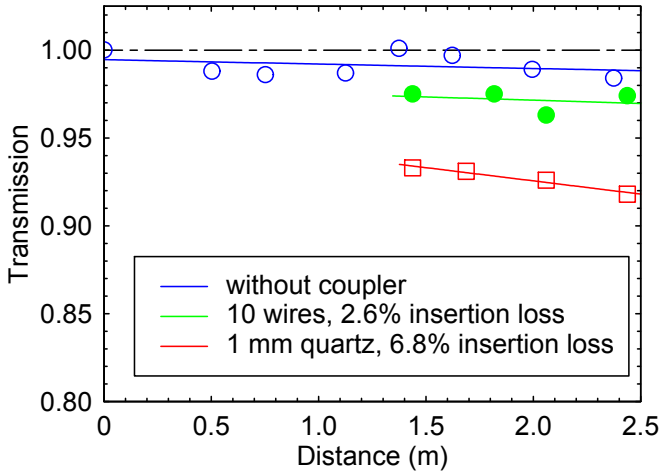

Fig. 21: Measured loss of the transmission line of Fig. 20

fabrication and alignment of the waveguide components. However, in practice, the loss may be dominated by the imperfections in the THz beam entering the transmission line and poor coupling of the beam to the line. When the output beam of the gyrotron is not a perfect Gaussian beam or the output beam is not perfectly matched (due to tilts and offsets) upon insertion into the waveguide, high losses may be found on the transmission line [86].

The transmission line shown in Fig. 19 has directional couplers for measuring forward and reverse power. They have been fabricated by stretching metal wires across the waveguide surface area and have only a 2.6% insertion loss, as shown in Fig. 21. This approach was found to be superior to using a quartz coupler. The transmission line of Fig. 19 has only one right angle bend and it is accomplished using two mirrors. The mirrors also match the beam from the 22 mm waveguide into the 8 mm waveguide used in the NMR probe. The smaller diameter waveguide in the probe is necessitated by the limited space in the probe. The bend may also be accomplished using a right angle bend, called a miter bend, in waveguide and by waveguide diameter tapers. Due to losses induced by imperfections in the Gaussian beam quality of the gyrotron and by errors in the alignment of the components of the transmission line, the transmission efficiency from the gyrotron output window to the sample is typically in the 50 to 80% range [74, 87].

The transmission line shown in Fig. 19 is only one example of successful transmission lines used in DNP NMR research. Recently, a very long transmission line using corrugated waveguides and switches has been successfully implemented on a 260 GHz gyrotron system for DNP NMR [88, 89]. A fully optical (mirror) transmission line using a mirror relay line has also recently been implemented for a DNP NMR spectrometer system [90]. Future research will concentrate on making these transmission lines simpler and more efficient.

V. Versatile Probes for DNP

MAS DNP probes can couple frequencies spanning eight orders of magnitude of the electromagnetic spectrum to samples under study. The DNP probe for experiments at a 9T magnetic field shown in Fig. 22 integrates an RF circuit that resonates an inductor surrounding the sample at 38, 96 and

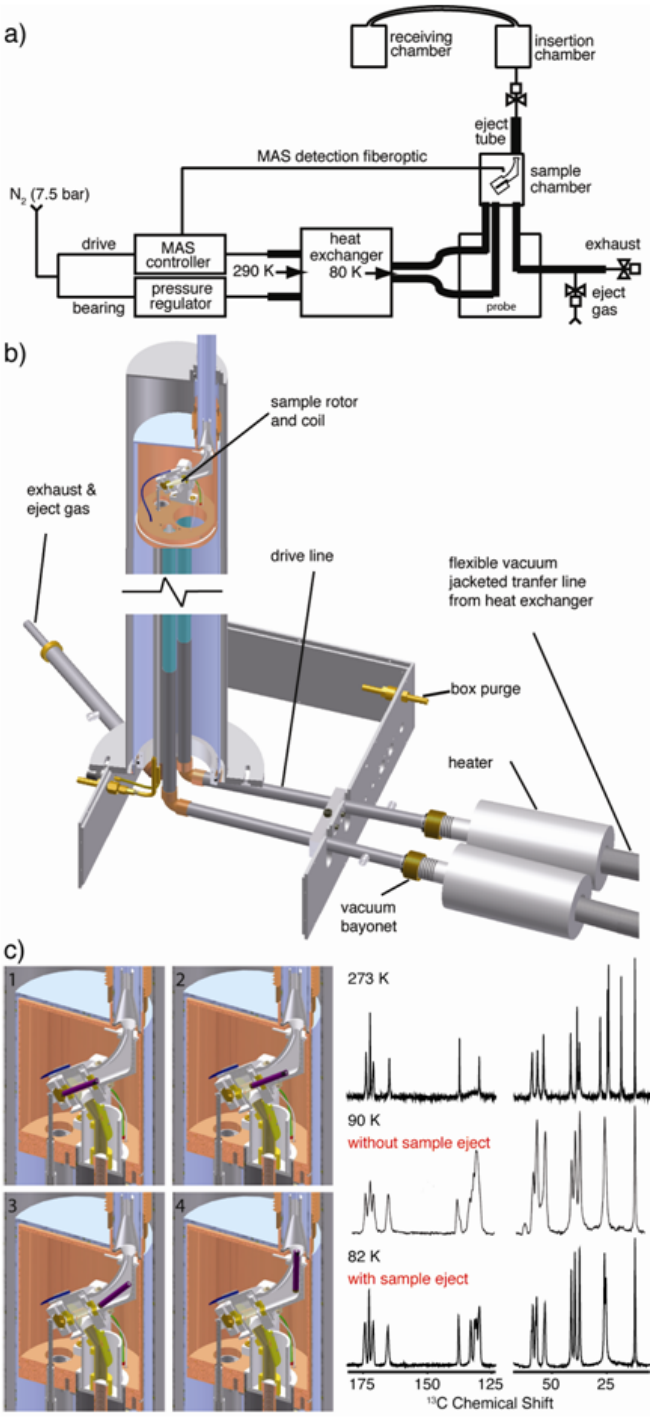

Fig. 22. Cryogenic MAS and sample exchange. a) Overview of the system architecture of the cryogenic sample spinning and exchange system. Thick black lines indicate vacuum jacketed transfer lines. b) Elements of the probe design required from cryogenic spinning. c) (left) the rotor ejecting from the spinning module (right) Spectra of a tripeptide at room temperature showing narrow lines at room temperature and with the cryogenic sample exchange, but broad unresolved spectrum without the sample exchange due to poorly optimized shims and the magic angle. (Adapted from [41]).

380 MHz to control and detect ^{15}N, ^{13}C, and ^{1}H spins, respectively. 250 GHz and 532 nm radiation channels illuminate the sample to excite the EPR and visible spectra[41]. Additionally, probes also house a pneumatic spinning module to mechanically rotate the sample at frequencies up to 8 KHz at an angle of 54.7^{o} (the Magic

Angle) with respect to the B_o NMR field. This motion partially averages anisotropic chemical shift and dipolar tensors that would otherwise result in broad NMR line shapes and poorly resolved spectra.

A. *Cryogenic Magic Angle Spinning*

Electron spin relaxation times, T_{1e}, in MAS DNP experiments increase at lower temperatures. Electron spins relaxing faster than the rate of transfer of polarization to the nuclear spins result in inefficient DNP transfers. Utilizing polarization agents with long (T_{1e}~1ms) longitudinal relaxation at ambient temperatures [22] is a strategy to circumvent this issue, and these T_{1e}'s are generally observed in radicals such as trityl with narrow powder patterns. However, these systems lead to a SE mechanism that does not scale well at higher magnetic fields. A more general strategy is to dope the sample with radicals that that have a larger g-anisotropy that supports the CE mechanism, and to perform the experiments at low temperatures (~90 K), where the relaxation times of both the electron and nuclear spins are longer. After the initial electron to nuclear polarization step, inherent proton spin-lattice relaxation mechanisms compete with the microwave driven polarization of the nuclear spins.

Achieving a uniform cryogenic sample temperature without exposing sensitive elements in the probe to a harsh environment is accomplished by thermally isolating the sample chamber and using the bearing and turbine gases needed for MAS spinning also as variable temperature cryogens [41]. A vacuum jacketed dewar (Fig. 22b) and the use of insulating material in the probe body reduces heat transfer from the sample chamber to the probe box and magnet bore which are maintained at ambient temperature.

In MAS DNP experiments, cooling to near 80 K can be achieved through a heat exchange process with liquid nitrogen. Since the DNP enhancement is extremely sensitive to temperature in the range of 80 K, the temperature typically must be regulated to within 0.5 K. Furthermore, the generation and trapping of photointermediates in photoactive proteins such as bR requires temperature control over a wide temperature range from 90 K – 273 K.[91]

B. *Cryogenic Sample Exchange*

During the operation of the 250 GHz / 380 MHz system at MIT, it was found that the time periods and effort required to change samples were longer and more arduous than anticipated. Specifically, because of the mass of the probe, it requires about three hours to warm the system, change samples, and re-cool to 85-90 K where the DNP experiment is performed. In addition, the magic angle and shim coils become misadjusted when the probe is physically moved out and back into the magnet. The THz transmission line can also be misaligned when the probe is moved. A system was developed to eject the sample from low temperatures and therefore avoid warming and cooling the probe [41], while at the same time retaining much better experimental stability. After sample exchange, the spinning frequency can be returned to ~7 KHz in about 10 minutes while re-establishing a temperature of 90 K in the sample chamber. The entire instrumental apparatus (gyrotron, probe, heat exchanger, etc.) has run for a two-month period without detrimental frost formation. Over 100 sample insertions and ejections have been performed over a one-year period without damage to a sapphire or zirconia rotor. In the same period, not a single rotor has been stuck in the stator preventing sample ejection, proving the robustness of this ejection system. The ejection process is depicted in Fig. 22c, along with spectra demonstrating the excellent resolution available at 82 K using a probe equipped with a cryogenic sample ejection system [41].

C. *RF circuit*

RF circuits such as that in Fig. 23 couple power from RF amplifiers and the NMR spectrometer to an inductor surrounding the sample. The quality factors of several hundred at the three resonant frequencies of the nuclear spins efficiently utilize the RF power and generate strong fields orthogonal to the main magnetic field of the superconducting

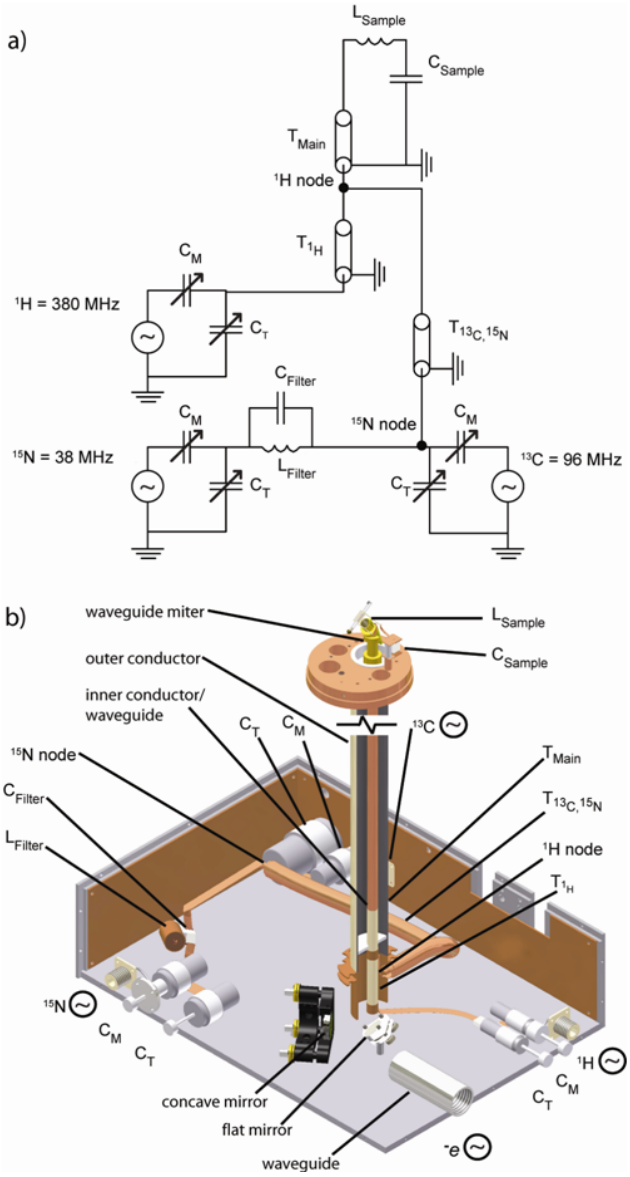

Fig. 23: RF circuit a) Circuit diagram showing transmission lines, sample inductor, isolation elements and variable tuning and matching capacitors. b) Solid model rendition of a typical RF circuit. (Adapted from [41])

NMR magnet. Isolation between the three RF ports is accomplished with LC and RC filters and branching off channels at high impedance points near current nodes. The tuning, matching, and isolation elements in the RF circuits can either be located near the coil or utilize a transmission line to physically separate the elements from the harsh cryogenic environment near the sample [92, 93].

D. THz coupling to sample

The sensitivity enhancement in DNP experiments depends strongly on the intensity of the millimeter waves in the sample of interest. Specifically, it is important to know the magnitude of the THz field, B_{1S}, that is orthogonal to B_0 and oscillates at the frequencies leading to polarization transfer. The THz beam is brought through the probe in a small diameter waveguide, as shown in Fig. 23. The waveguide serves as both the inner conductor for the RF transmission line and the corrugated waveguide for the THz transmission. The THz radiation is launched from the end of the corrugated waveguide. The beam that is launched has a Gaussian power distribution generated from the HE_{11} mode of the corrugated transmission line, as shown in Fig. 19. However, the RF coil, large sample volume, and other physical requirements of the MAS NMR experiment hinder the illumination of the sample with the THz waves.

Recently, High Frequency Structure Simulator (HFSS) was used to calculate how the THz radiation travels from the antenna, diffracts through the coil, and is distributed across the sample, as shown in Fig. 24 [74]. For the 2.4 mm diameter sample held in a 4 mm sapphire rotor, the calculated average B_{1S} THz field is $13\mu T/W^{1/2}$, although the magnitude varies quite drastically across the sample due to diffraction effects.

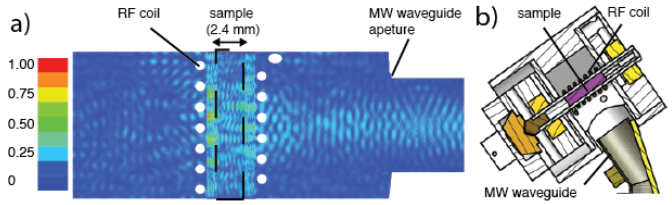

Fig. 24. THz coupling to sample. a) HFSS calculation of the THz wave intensity throughout the sample and spinning chamber. b) solid model depicting the THz antenna, spinning module, and sample. (Adapted from [74]).

The enhancement observed in a DNP CE experiment can be described using the calculated B_{1S} and a simplified expression for the steady state enhancement derived by Wollan [94]. Since the microwave field, $\omega_{1S}=\gamma_S B_{1S}$, is inhomogeneous, as demonstrated in Fig. 24, the expression must be integrated over the field dependence for the sample volume

$$\varepsilon = \frac{1}{V}\varepsilon_{max}\int \frac{\alpha\left(\frac{\omega_{1S}}{2\pi}\right)^2}{1+\alpha\left(\frac{\omega_{1S}}{2\pi}\right)^2}dV \qquad (4)$$

where $\alpha = (T_{1S}T_{2S})/2$. The factor of 1/2 converts from the time averaged linearly polarized ω_{1S}^2 to the time averaged circularly polarized component that interacts with the electrons. T_{1S} for a Nitroxide radical is expected to range from 10-400 μs in the 90 Kelvin temperature regime, and T_{2S} is a strong function of radical concentration being in the range of 10 to 200 ns for the 20 mM electron concentration in our sample. The magnitude of the product $T_{1S}T_{2S}\omega_{1S}^2 << 1$ to obtain the quadratic dependence observed at low ω_{1S}^2. It then saturates at high ω_{1S}^2. Fig. 25 is a plot of the experimental enhancement of 1 M ^{13}C-urea and 10 mM TOTAPOL dissolved in d_8-glycerol/D_20/H_20 (60/30/10% by volume) [95, 96] vs. $\omega_1/2\pi$ at 250 GHz for the sample and probe described in Figs. 22 and 23 and the field distribution shown in Fig. 24. An excellent fit to the experimental data is obtained for the parameters $\varepsilon_{max} = 230$, $T_{1S}T_{2S}=8\times10^{-12}$ s^2. Calculating the value of $\gamma_S B_{1S}$ at the level of a mesh element volume defined by the HFSS model is crucial to understanding the DNP enhancement data and, indeed, to modeling the enhancement more generally obtained from the cross effect [94].

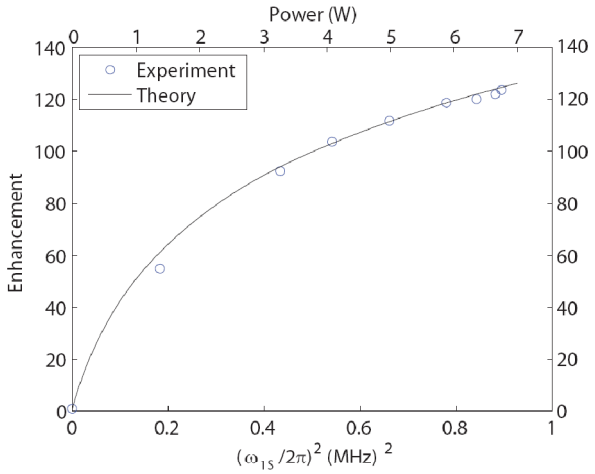

Fig. 25. DNP enhancement vs. $\omega_{1S}/2\pi$(bottom) and power (top) for a fully packed rotor of 1 M ^{13}C-urea and 10 mM TOTAPOL dissolved in d_8-glycerol/D_20/H_20 (60/30/10% by volume). (Adapted from [74]).

VI. Conclusions

Dynamic Nuclear Polarization has become firmly established as a powerful technique for enhancing signal intensities in NMR spectroscopy. In DNP NMR, the required frequencies for microwave irradiation of the sample have increased as NMR has moved to progressively higher magnetic fields due to the improved resolution and sensitivity. Modern NMR spectrometers are presently operating at proton frequencies close to 1 GHz, corresponding to fields of 23 T. The microwave frequencies needed for these spectrometers enter the terahertz regime as the magnetic field exceeds 10.7 T. Stated another way, for NMR spectrometers operating above 450 MHz, the required microwave frequency for DNP NMR is in the terahertz range.

The gyrotron is capable of achieving the power and stability requirements for THz DNP NMR. The number of gyrotron-based DNP NMR systems was only a single system in 1990 and increased to two systems only in 2000 (both at MIT). However, as pointed out by Griffin and Prisner [8], DNP NMR is now enjoying a renaissance. There are now approximately 20 THz DNP NMR systems either operating or under construction and more systems will surely follow. THz DNP NMR will thus be recognized as a major present-day application of THz technology.

Further utilization of THz DNP NMR will likely be strongly coupled to advances in THz technology. The THz source power level of ten to one hundred Watts needed for THz DNP NMR is currently only achievable by gyrotrons. One can however envision the possibility of achieving the required power levels at THz frequencies with advanced versions of klystrons or traveling wave tubes. These might bring down the cost and complexity of the THz DNP NMR system. When coupled with commercial development, THz DNP NMR could become the preferred approach to many solid and liquid state NMR experiments.

VII. Acknowledgments

This research was supported by the National Institutes of Health through grants EB001965, EB004866, EB001960, EB002804, EB003151, and EB002026. A.B.B. was partially supported by graduate research fellowship from the National Science Foundation.

VIII. References

[1] A. Abragam and M. Goldman, "Principles of dynamic nuclear polarisation," *Reports on Progress in Physics,* vol. 41, p. 395, 1978.

[2] A. W. Overhauser, "Polarization of Nuclei in Metals," *Phys. Rev.,* vol. 92, pp. 411-415, 1953.

[3] T. R. Carver and C. P. Slichter, "Polarization of Nuclear Spins in metals," *Physical Review,* vol. 92, pp. 212-213, 1953.

[4] A. Abragam and W. G. Proctor, "A novel method of dynamic polarization of atomic nuclei in solids," *CR Acad. Sci,* vol. 246, 1959.

[5] M. Afeworki, R. A. Mckay, and J. Schaefer, "Selective Observation of the Interface of Heterogeneous Polycarbonate Polystyrene Blends by Dynamic Nuclear-Polarization C-13 Nmr-Spectroscopy," *Macromolecules,* vol. 25, pp. 4084-4091, AUG 3 1992.

[6] D. J. Singel, H. Seidel, R. D. Kendrick, and C. S. Yannoni, "A Spectrometer for EPR, DNP, and Multinuclear High-Resolution NMR," *Journal of Magnetic Resonance,* vol. 81, pp. 145-161, 1989.

[7] R. A. Wind, M. J. Duijvestijn, C. Vanderlugt, A. Manenschijn, and J. Vriend, "Applications of Dynamic Nuclear-Polarization in C-13 Nmr in Solids," *Progress in Nuclear Magnetic Resonance Spectroscopy,* vol. 17, pp. 33-67, 1985.

[8] R. G. Griffin and T. F. Prisner, "High field dynamic nuclear polarization - the renaissance," *Physical Chemistry Chemical Physics,* vol. 12, pp. 5737-5740, 2010.

[9] L. R. Becerra, G. J. Gerfen, R. J. Temkin, D. J. Singel, and R. G. Griffin, "Dynamic Nuclear Polarization with a Cyclotron Resonance Maser at 5 T," *Physical Review Letters,* vol. 71, pp. 3561-3564, 1993.

[10] V. S. Bajaj, C. T. Farrar, M. K. Hornstein, I. Mastovsky, J. Vieregg, J. Bryant, B. Elena, K. E. Kreischer, R. J. Temkin, and R. G. Griffin, "Dynamic nuclear polarization at 9T using a novel 250 GHz gyrotron microwave source," *J. Mag. Res.,* vol. 160, pp. 85-90, 2003.

[11] M. K. Hornstein, V. S. Bajaj, R. G. Griffin, K. E. Kreischer, I. Mastovsky, M. A. Shapiro, J. R. Sirigiri, and R. J. Temkin, "Second harmonic operation at 460 GHz and broadband continuous frequency tuning of a gyrotron oscillator," *Electron Devices, IEEE Transactions on,* vol. 52, pp. 798-807, 2005.

[12] A. C. Torrezan, H. Seong-Tae, M. A. Shapiro, J. R. Sirigiri, and R. J. Temkin, "CW operation of a tunable 330/460 GHz gyrotron for enhanced nuclear magnetic resonance," in *Infrared, Millimeter and Terahertz Waves, 2008. IRMMW-THz 2008. 33rd International Conference on*, 2008, pp. 1-2.

[13] V. Denysenkov, M. J. Prandolini, M. Gafurov, D. Sezer, B. Endeward, and T. F. Prisner, "Liquid state DNP using a 260 GHz high power gyrotron," *Physical Chemistry Chemical Physics,* vol. 12, pp. 5786-5790, 2010.

[14] Ü. Akbey, W. T. Franks, A. Linden, S. Lange, R. G. Griffin, B.-J. van Rossum, and H. Oschkinat, "Dynamic Nuclear Polarization of Deuterated Proteins," *Angewandte Chemie International Edition,* vol. 49, pp. 7803-7806, 2010.

[15] Y. Matsuki, H. Takahashi, K. Ueda, T. Idehara, I. Ogawa, M. Toda, H. Akutsu, and T. Fujiwara, "Dynamic nuclear polarization experiments at 14.1 T for solid-state NMR," *Physical Chemistry Chemical Physics,* vol. 12, pp. 5799-5803, 2010.

[16] M. Rosay, L. Tometich, S. Pawsey, R. Bader, R. Schauwecker, M. Blank, P. M. Borchard, S. R. Cauffman, K. L. Felch, R. T. Weber, R. J. Temkin, R. G. Griffin, and W. E. Maas, "Solid-state dynamic nuclear polarization at 263 GHz: spectrometer design and experimental results," *Physical Chemistry Chemical Physics,* vol. 12, pp. 5850-5860.

[17] V. Vitzthum, M. A. Caporini, and G. Bodenhausen, "Solid-state nitrogen-14 nuclear magnetic resonance enhanced by dynamic nuclear polarization using a gyrotron," *Journal of Magnetic Resonance,* vol. 205, pp. 177-179, 2010.

[18] K.-N. Hu, V. S. Bajaj, M. M. Rosay, and R. G. Griffin, "High Frequency Dynamic Nuclear Polarization Using Mixtures of TEMPO and Trityl Radicals," *J. Chem. Phys.,* vol. 126, p. 044512, 2007.

[19] Y. Matsuki, T. Maly, O. Ouari, H. Karoui, F. Le Moigne, E. Rizzato, S. Lyubenova, J. Herzfeld, T. Prisner, P. Tordo, and R. Griffin, "Dynamic Nuclear Polarization with a Rigid Biradical," *Angewandte Chemie,* vol. 121, pp. 5096-5100, 2009.

[20] C.-G. Joo, K.-N. Hu, J. A. Bryant, and R. G. Griffin, "*In Situ* Temperature Jump High-Frequency Dynamic Nuclear Polarization Experiments: Enhanced Sensitivity in Liquid-State NMR Spectroscopy," *J. Am Chem. Soc,* vol. 128, pp. 9428-9432, 2006.

[21] M. Afeworki, R. a. Mckay, and J. Schaefer, "Dynamic Nuclear-Polarization Enhanced Nuclear-Magnetic-Resonance of Polymer-Blend Interfaces," *Materials Science and Engineering a-Structural*

Materials Properties Microstructure and Processing, vol. 162, pp. 221-228, APR 30 1993.

[22] M. Afeworki and J. Schaefer, "Mechanism of DNP-Enhanced Polarization Transfer Across the Interface of Polycarbonate/Polystyrene Heterogeneous Blends," *Macromolecules,* vol. 25, pp. 4092-4096, 1992.

[23] M. Afeworki and J. Schaefer, "Molecular Dynamics of Polycarbonate Chains at the Interface of Polycarbonate/Polystyrene Heterogeneous Blends," *Macromolecules,* vol. 25, pp. 4097-4099, 1992.

[24] M. Afeworki, S. Vega, and J. Schaefer, "Direct Electron-to-Carbon Polarization Transfer in Homgeneously-Doped Polycarbonates," *Macromolecules,* vol. 25, pp. 4100-4106, 1992.

[25] G. J. Gerfen, L. R. Becerra, D. A. Hall, R. G. Griffin, R. J. Temkin, and D. J. Singel, "High-Frequency (140 Ghz) Dynamic Nuclear-Polarization - Polarization Transfer to a Solute in Frozen Aqueous-Solution," *Journal of Chemical Physics,* vol. 102, pp. 9494-9497, Jun 1995.

[26] M. Rosay, V. Weis, K. E. Kreischer, R. J. Temkin, and R. G. Griffin, "Two-dimensional ^{13}C-^{13}C correlation spectroscopy with magic angle spinning and dynamic nuclear polarization," *Journal of the American Chemical Society,* vol. 124, pp. 3214-3215, Apr 3 2002.

[27] M. Rosay, J. C. Lansing, K. C. Haddad, W. W. Bachovchin, J. Herzfeld, R. J. Temkin, and R. G. Griffin, "High Frequency Dynamic Nuclear Polarization in MAS Spectra of Membrane and Soluble Proteins," *J. Am. Chem. Soc.,* vol. 125, pp. 13626-27, 2003.

[28] V. S. Bajaj, M. K. Hornstein, K. E. Kreischer, J. R. Sirigiri, P. P. Woskov, M. L. Mak-Jurkauskas, J. Herzfeld, R. J. Temkin, and R. G. Griffin, "250 GHz CW gyrotron oscillator for dynamic nuclear polarization in biological solid state NMR," *Journal of Magnetic Resonance,* vol. 189, pp. 251-279, Dec 2007.

[29] T. Maly, G. T. Debelouchina, V. S. Bajaj, K.-N. Hu, C.-G. Joo, M. L. Mak-Jurkauskas, J. R. Sirigiri, P. C. A. v. d. Wel, J. Herzfeld, R. J. Temkin, and R. G. Griffin, "Dynamic Nuclear Polarization at High Magnetic Fields," *J. Chem Physics,* vol. 128, p. 052211, 2008.

[30] M. Goldman, *Spin Temperature and Nuclear Magnetic Resonance in Solids*. London: Oxford University Press, 1970.

[31] K.-N. Hu, H.-h. Yu, T. M. Swager, and R. G. Griffin, "Dynamic nuclear polarization with biradicals," *J. Am. Chem. Soc.,* vol. 126, pp. 10844-10845, Sep 2004.

[32] V. A. Atsarkin, "Dynamic Polarization of Nuclei in Solid Dielectrics," *Soviet Physics Solid State,* vol. 21, pp. 725-744, 1978.

[33] P. C. A. van der Wel, K.-N. Hu, J. R. Lewandowski, and R. G. Griffin, "Dynamic Nuclear Polarization of Amyloidogenic Peptide Nanocrystals: GNNQQNY, a Core Segment of the Yeast Prion Protein Sup35p " *J. Am. Chem. Soc.,* vol. 128, pp. 10840-10846, 2006.

[34] P. C. A. van der Wel, J. Lewandoswki, and R. G. Griffin, "Solid state NMR study of amyloid nanocrystals and fibrils formed by the peptide GNNQQNY from yeast prion protein Sup35p," *J. Am Chem. Soc,* vol. 128, pp. 10840-10846, 2007.

[35] G. Debelouchina, M. Bayro, P. van der Wel, M. Caporini, A. Barnes, M. Rosay, W. Maas, and R. Griffin, "Dynamic nuclear polarization-enhanced solid-state NMR spectroscopy of GNNQQNY nanocrystals and amyloid fibrils," *Phys. Chem. Chem. Phys.,* vol. 12, pp. 5911-5919, 2010.

[36] M. Rosay, A. C. Zeri, N. S. Astrof, S. J. Opella, J. Herzfeld, and R. G. Griffin, "Sensitivity-enhanced NMR of biological solids: Dynamic nuclear polarization of Y21M fd bacteriophage and purple membrane," *Journal of the American Chemical Society,* vol. 123, pp. 1010-1011, Feb 7 2001.

[37] A. Lesage, M. Lelli, D. Gajan, M. A. Caporini, V. Vitzthum, P. Mieville, J. Alauzun, A. Roussey, C. Thieuleux, A. Mehdi, G. Bodenhausen, C. Coperet, and L. Emsley, "Surface Enhanced NMR Spectroscopy by Dynamic Nuclear Polarization," *Journal of the American Chemical Society,* vol. 132, pp. 15459-15461, Nov.

[38] R. Tycko, "Progress towards a molecular-level structural understanding of amyloid fibrils," *Current Opinion in Structural Biology,* vol. 14, pp. 96-103, FEB 2004.

[39] F. Chiti and C. M. Dobson, "Protein Misfolding, Functional Amyloid, and Human Disease," *Annual Review of Biochemistry,* vol. 75, pp. 333-366, 2006.

[40] C. P. Jaroniec, C.E. MacPhee, N.S. Astrof, C.M. Dobson, R.G. Griffin,, "Molecular Conformation of a Peptide Fragment of Transthyretin in an Amyloid Fibril," *Proc. Nat'l. Acad. Sci.,* vol. 99,, pp. 16748-16753, 2002.

[41] A. B. Barnes, M. L. Mak-Jurkauskas, Y. Matsuki, V. S. Bajaj, P. C. A. van der Wel, R. DeRocher, J. Bryant, J. R. Sirigiri, R. J. Temkin, J. Lugtenburg, J. Herzfeld, and R. G. Griffin, "Cryogenic sample exchange NMR probe for magic angle spinning dynamic nuclear polarization," *J. Mag. Res.,* vol. 198, pp. 261-270, Jun 2009.

[42] J. M. Griffiths, K. V. Lakshmi, A. E. Bennett, J. Raap, C. M. Vanderwielen, J. Lugtenburg, J. Herzfeld, and R. G. Griffin, "Dipolar Correlation NMR-Spectroscopy of a Membrane-Protein," *J. Am. Chem. Soc.,* vol. 116, pp. 10178-10181, 1994.

[43] V. Bajaj, M. Mak-Jurkauskas, M. Belenky, J. Herzfeld, and R. Griffin, "Functional and shunt states of bacteriorhodopsin resolved by 250 GHz dynamic nuclear polarizationñenhanced solid-state NMR," *Proc. Natl. Acad. Sci.,* vol. 106, p. 9244, 2009.

[44] J. K. Lanyi and B. Schobert, "Crystallographic structure of the retinal and the protein after deprotonation of the Schiff base: The switch in the bacteriorhodopsin photocycle," *Journal of Molecular Biology,* vol. 321, pp. 727-737, AUG 23 2002.

[45] A. B. Barnes, B. Corzilius, M. L. Mak-Jurkauskas, L. B. Andreas, V. S. Bajaj, Y. Matsuki, M. L. Belenky, J. Lugtenburg, J. R. Sirigiri, R. J. Temkin, J. Herzfeld, and R. G. Griffin, "Resolution and polarization distribution in cryogenic DNP/MAS experiments," *Physical Chemistry Chemical Physics,* vol. 12, pp. 5861-5867, 2010.

[46] V. L. Granatstein, R. K. Parker, and C. M. Armstrong, "Vacuum electronics at the dawn of the twenty-first century," *Proceedings of the IEEE,* vol. 87, pp. 702-716, 1999.

[47] K. R. Thurber, W.-M. Yau, and R. Tycko, "Low-temperature dynamic nuclear polarization at 9.4 T with a 30 mW microwave source," *Journal of Magnetic Resonance,* vol. 204, pp. 303-313, 2010.

[48] V. Weis, M. Bennati, M. Rosay, J. A. Bryant, and R. G. Griffin, "High-Field DNP and ENDOR with a Novel Multiple-Frequency Resonance Structure," *Journal of Magnetic Resonance,* vol. 140, pp. 293-299, 1999.

[49] M. J. Prandolini, V. P. Denysenkov, M. Gafurov, S. Lyubenova, B. Endeward, M. Bennati, and T. F. Prisner, "First DNP Results from a Liquid Water-TEMPOL Sample at 400 MHz and 260 GHz," *Applied Magnetic Resonance,* vol. 34, pp. 399-407, 2008.

[50] A. Roitman, D. Berry, and B. Steer, "State-of-the-art W-band extended interaction klystron for the CloudSat program," *Electron Devices, IEEE Transactions on,* vol. 52, pp. 895-898, 2005.

[51] B. Steer, M. Hyttinen, A. Roitman, P. Horoyski, G. M. Smith, D. R. Bolton, P. A. S. Cruickshank, and D. A. Robertson, "Compact, high power EIK sources used for ESR and NMR," in *Infrared, Millimeter and Terahertz Waves, 2008. IRMMW-THz 2008. 33rd International Conference on*, 2008, pp. 1-2.

[52] K. L. Felch, B. G. Danly, H. R. Jory, K. E. Kreischer, W. Lawson, B. Levush, and R. J. Temkin, "Characteristics and applications of fast-wave gyrodevices," *Proceedings of the IEEE,* vol. 87, pp. 752-781, 1999.

[53] G. S. Nusinovich, "Introduction to the Physics of Gyrotrons," *Johns Hopkins University Press,* 2004.

[54] V. E. Zapevalov, V. V. Dubrov, A. S. Fix, E. A. Kopelovich, A. N. Kuftin, O. V. Malygin, V. N. Manuilov, M. A. Moiseev, A. S. Sedov, N. P. Venediktov, and N. A. Zavolsky, "Development of 260 GHZ second harmonic CW gyrotron with high stability of output parameters for dnp spectroscopy," in *Infrared, Millimeter, and Terahertz Waves, 2009. IRMMW-THz 2009. 34th International Conference on*, 2009, pp. 1-2.

[55] K. Kosuga, T. Idehara, I. Ogawa, T. Saito, L. Agusu, T. Kanemaki, M. E. Smith, and R. Dupree, "Development of gyrotron FU CW VII for 600 and 300 MHz DNP-NMR," in *Infrared, Millimeter, and Terahertz Waves, 2009. IRMMW-THz 2009. 34th International Conference on*, 2009, pp. 1-2.

[56] A. C. Torrezan, M. A. Shapiro, J. R. Sirigiri, R. J. Temkin, and R. G. Griffin, "Operation of a Continuously Frequency-Tunable Second-Harmonic CW 330-GHz Gyrotron for Dynamic Nuclear Polarization," *Electron Devices, IEEE Transactions on,* vol. (Submitted for Publication), 2011.

[57] B. G. Danly and R. J. Temkin, "Generalized nonlinear harmonic gyrotron theory," *Physics of Fluids,* vol. 29, p. 561, 1986.

[58] J. Schneider, uuml, and rgen, "Stimulated Emission of Radiation by Relativistic Electrons in a Magnetic Field," *Physical Review Letters,* vol. 2, p. 504, 1959.

[59] A. Gapanov, "Addendum izvestia," *Izv. VUZ. Radiofizika,* vol. 2, pp. 450-462, 1959.

[60] J. L. Hirshfield and J. M. Wachtel, "1964," *Phys. Rev. Lett.,* vol. 12, Electron Cyclotron Maser.

[61] R. J. Temkin, K. E. Kreischer, W. J. Mulligan, S. MacCabe, and H. R. Fetterman, "A 100 kW, 140 GHz pulsed gyrotron," *International Journal of Infrared and Millimeter Waves,* vol. 3, pp. 427-437, 1982.

[62] S. Spira-Hakkarainen, K. E. Kreischer, and R. J. Temkin, "Submillimeter-wave harmonic gyrotron experiment," *Plasma Science, IEEE Transactions on,* vol. 18, pp. 334-342, 1990.

[63] T. Notake, T. Saito, Y. Tatematsu, A. Fujii, S. Ogasawara, L. Agusu, I. Ogawa, T. Idehara, and V. N. Manuilov, "Development of a Novel High Power Sub-THz Second Harmonic Gyrotron," *Physical Review Letters,* vol. 103, p. 225002, 2009.

[64] T. L. Grimm, K. E. Kreischer, and R. J. Temkin, "Experimental study of a megawatt 200-300 GHz gyrotron oscillator," *Physics of Fluids B,* vol. 5, pp. 4135-4143, 1993.

[65] G. F. Brand, Z. Chen, N. G. Douglas, M. Gross, J. Y. L. Ma, and L. C. Robinson, "A Tunable Millimeter Submillimeter Gyrotron," *Intl. J. Electron.,* vol. 57, 1984.

[66] T. Idehara, I. Ogawa, H. Mori, S. Kobayashi, S. Mitsudo, and T. Saito, "A THz Gyrotron FU CW III with a 20T superconducting magnet," in *Infrared, Millimeter and Terahertz Waves, 2008. 33rd International Conference on*, 2008, pp. 1-2.

[67] T. Idehara, S. Misudo, and I. Ogawa, "Development of high-frequency, highly stable gyrotrons as millimeter to submillimeter wave radiation sources," *IEEE Trans. Plasma Sci.,* vol. 32, 2004.

[68] J. H. Booske, R. Dobbs, and C. D. J. e. al., "Vacuum Electronic Sources for High Power Terahertz-Regime Radiation (this issue) " *IEEE Trans. THz Sci. Tech.,* 2011.

[69] C. D. Joye, R. G. Griffin, M. K. Hornstein, H. Kan-Nian, K. E. Kreischer, M. Rosay, M. A. Shapiro, J. R. Sirigiri, R. J. Temkin, and P. P. Woskov, "Operational characteristics of a 14-W 140-GHz gyrotron for dynamic nuclear polarization," *Plasma Science, IEEE Transactions on,* vol. 34, pp. 518-523, 2006.

[70] S. T. Han, R. G. Griffin, K.-N. Hu, C.-G. Joo, C. D. Joye, I. Mastovsky, M. A. Shapiro, J. R. Sirigiri, R. J. Temkin, A. C. Torrezan, and P. P. Woskov,

"Continuous-wave Submillimeter-wave Gyrotrons," *Proc. of SPIE,* vol. 6373, p. 63730C, 2006.

[71] S. T. Han, C. D. Joye, L. Mastovsky, M. A. Shapiro, J. R. Sirigiri, R. J. Temkin, and P. P. Woskov, "Stable operation of a 0.46 THz continuous wave gyrotron oscillator," *2006 IEEE International Vacuum Electronics Conference,* p. 06EX1278, 2006.

[72] K. Kreischer, C. Farrar, R. Griffin, R. Temkin, and J. Vieregg, "A 250 GHz gyrotron for NMR spectroscopy," in *Plasma Science, 2000. ICOPS 2000. IEEE Conference Record - Abstracts. The 27th IEEE International Conference on*, 2000, p. 198.

[73] P. P. Woskov, V. S. Bajaj, M. K. Hornstein, R. J. Temkin, and R. G. Griffin, "Corrugated waveguide and directional coupler for CW 250-GHz gyrotron DNP experiments," *Microwave Theory and Techniques, IEEE Transactions on,* vol. 53, pp. 1863-1869, 2005.

[74] E. A. Nanni, A. B. Barnes, Y. Matsuki, P. P. Woskov, B. Corzilius, R. G. Griffin, and R. J. Temkin, "Microwave Field Distribution in a Magic Angle Spinning Dynamic Nuclear Polarization NMR Probe," *Journal of Magnetic Resonance,* vol. In Press, Accepted Manuscript.

[75] M. K. Hornstein, V. S. Bajaj, R. G. Griffin, and R. J. Temkin, "Continuous-wave operation of a 460-GHz second harmonic gyrotron oscillator," *IEEE Trans. Plasma Science,* vol. 34, pp. 524-533, 2006.

[76] V. Denysenkov, V. K. Kiseliov, M. Prandolini, M. Gafurov, A. Krahn, F. Engelke, V. I. Bezborodov, Y. M. Kuleshov, P. K. Nesterov, M. S. Yanovsky, and T. F. Prisner, "260 GHz quasioptical setup for EPR and DNP experiments on the 9.2 Tesla DNP/NMR/EPR spectrometer," *Physics and Engineering of Microwaves, Millimeter and Submillimeter Waves (MSMW), 2010 International Kharkov Symposium on,* pp. 1-7, 2010.

[77] R. Ikeda, T. Idehara, I. Ogawa, K. Kosuga, T. Saito, Y. Matsuki, K. Ueda, T. Fujiwara, and T. H. Chang, "Development of continuously frequency tunable gyrotrons FU CW VI and FU CW VI A for application to 600 MHz DNP-NMR spectroscopy," in *Infrared Millimeter and Terahertz Waves (IRMMW-THz), 2010 35th International Conference on*, 2010, pp. 1-2.

[78] E. Choi, M. Shapiro, J. Sirigiri, and R. Temkin, "Calculation of Radiation from a Helically Cut Waveguide for a Gyrotron Mode Converter in the Quasi-Optical Approximation," *Journal of Infrared, Millimeter and Terahertz Waves,* vol. 30, pp. 8-25, 2009.

[79] J. M. Neilson and R. Bunger, "Surface integral equation analysis of quasi-optical launchers," *Plasma Science, IEEE Transactions on,* vol. 30, pp. 794-799, 2002.

[80] A. C. Torrezan, H. Seong-Tae, I. Mastovsky, M. A. Shapiro, J. R. Sirigiri, R. J. Temkin, A. B. Barnes, and R. G. Griffin, "Continuous-Wave Operation of a Frequency-Tunable 460-GHz Second-Harmonic Gyrotron for Enhanced Nuclear Magnetic Resonance," *Plasma Science, IEEE Transactions on,* vol. 38, pp. 1150-1159, 2010.

[81] J. Harrington and e. al., "THz Waveguides with Low Loss," *IEEE Trans. THz Sci. Tech.,* vol. (this issue), 2011.

[82] P. Bhartia and I. J. Bahl, "Millimeter Wave Engineering and Applications," *John Wiley and Sons, New York, Chapter 5 – Transmission Lines 1 – Waveguides,* 1984.

[83] M. K. Thumm and W. Kasparek, "Passive high-power microwave components," *Plasma Science, IEEE Transactions on,* vol. 30, pp. 755-786, 2002.

[84] J. L. Doane, *Propagation and mode coupling in corrugated and smooth-walled circular waveguides* vol. 13. New York, Academic Press, 1985.

[85] E. J. Kowalski, D. S. Tax, M. A. Shapiro, J. R. Sirigiri, R. J. Temkin, T. S. Bigelow, and D. A. Rasmussen, "Linearly Polarized Modes of a Corrugated Metallic Waveguide," *Microwave Theory and Techniques, IEEE Transactions on,* vol. 58, pp. 2772-2780, 2010.

[86] M. A. Shapiro, E. J. Kowalski, J. R. Sirigiri, D. S. Tax, R. J. Temkin, T. S. Bigelow, J. B. Caughman, and D. A. Rasmussen, "Loss estimate for ITER ECH transmission line including multimode propagation," *Fusion Sci. and Tech.,* vol. 57, pp. 196-207, 2010.

[87] P. W. Woskov, V. S. Bajaj, M. K. Hornstein, R. J. Temkin, and R. G. Griffin, "Corrugated Waveguide and Directional Coupler for CW 250 GHz Gyrotron DNP Experiments," *IEEE Transactions on Microwave Theory and Techniques,* vol. 53, pp. 1863-69, 2005.

[88] A. A. Bogdashov, V. I. Belousov, A. V. Chirkov, G. G. Denisov, S. Y. Kornishin, and E. M. Tai, "Transmission line for 258 GHz gyrotron DNP spectroscopy," in *Infrared Millimeter and Terahertz Waves (IRMMW-THz), 2010 35th International Conference on*, 2010, pp. 1-2.

[89] G. Denisov, A. Chirkov, V. Belousov, A. Bogdashov, G. Kalynova, D. Sobolev, Y. Rodin, E. Tai, V. Ilin, S. Kornishin, M. Kulygin, V. Malygin, E. Soluyanova, V. Parshin, and M. Shmelev, "Millimeter Wave Multi-mode Transmission Line Components," *Journal of Infrared, Millimeter and Terahertz Waves,* pp. 1-15, 2011.

[90] I. Ogawa, T. Idehara, M. Myodo, H. Ando, D. Wagner, and M. Thumm, "Development of a Quasi-optical Transmission System for Gyrotron Application as a Radiation Source," in *Infrared Millimeter Waves and 14th International Conference on Teraherz Electronics, 2006. IRMMW-THz 2006. Joint 31st International Conference on*, 2006, pp. 552-552.

[91] M. L. Mak-Jurkauskas, V. S. Bajaj, M. K. Hornstein, M. Belenky, R. J. Temkin, R. G. Griffin, and J. Herzfeld, "Energy Transformations Early in the Bacteriorhodopsin Photocycle Revealed by DNP-Enhanced Solid State NMR," *Proceedings of the National Academy of Sciences of the United States of America,* vol. 105, pp. 883-888, 2008.

[92] R. A. McKay, "U.S. Patent #4,446,431," ed, 1984.
[93] R. A. McKay, "Probes for Special Purposes," in *Encyclopedia of Nuclear Magnetic Resonance*. vol. 6, D. M. Grant and R. Harris, Eds., ed New York: John Wiley and Sons, 1996, pp. 3768-71.
[94] D. S. Wollan, "Dynamic Nuclear Polarization with an Inhomogeneously Broadened ESR Line. I Theory," *Phys. Rev. B,* vol. 13, pp. 3671-3685, 1976.
[95] K.-N. Hu, C. Song, H.-h. Yu, T. M. Swager, and R. G. Griffin, "High-Frequency Dynamic Nuclear Polarization Using Biradicals: A Multifrequency EPR Lineshape Analysis," *J. Chem. Phys.,* vol. 128, p. 052321, 2008.
[96] C. Song, K.-N. Hu, C.-G. Joo, T. M. Swager, and R. G. Griffin, "TOTAPOL – A Biradical Polarizing Agent for Dynamic Nuclear Polarization Experiments in Aqueous Media," *J. Am Chem. Soc,* vol. 128, pp. 11385-90, 2006.